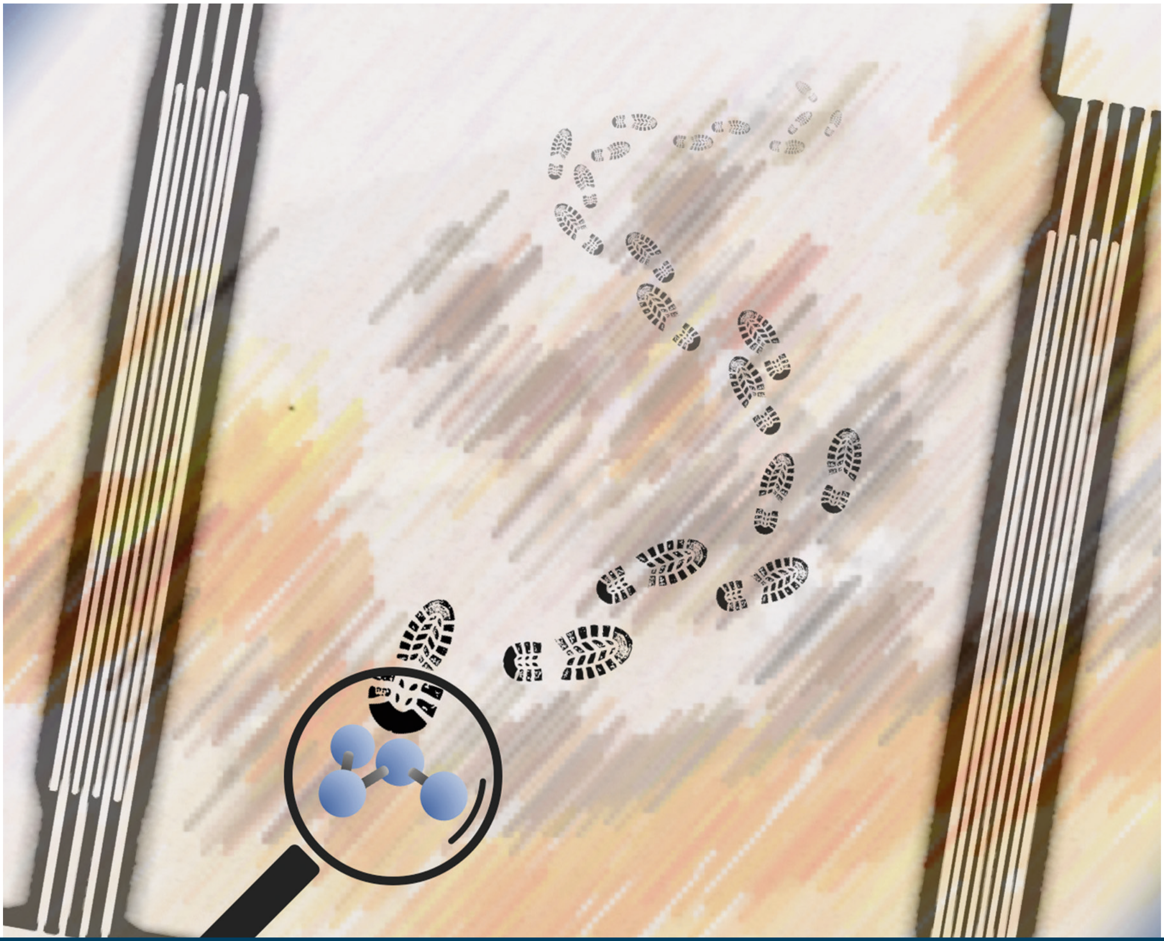

Development of a surface acoustic wave sensor for in situ detection of molecules

Dennis Finck

Schlüsseltechnologien / Key Technologies
Band / Volume 216
ISBN 978-3-95806-464-5

Mitglied der Helmholtz-Gemeinschaft

JÜLICH
Forschungszentrum

Schriften des Forschungszentrums Jülich
Reihe Schlüsseltechnologien / Key Technologies Band / Volume 216

Forschungszentrum Jülich GmbH
Institute of Complex Systems
Bioelectronics (ICS-8)

Development of a surface acoustic wave sensor for in situ detection of molecules

Dennis Finck

Schriften des Forschungszentrums Jülich
Reihe Schlüsseltechnologien / Key Technologies Band / Volume 216

ISSN 1866-1807 ISBN 978-3-95806-464-5

Bibliografische Information der Deutschen Nationalbibliothek.
Die Deutsche Nationalbibliothek verzeichnet diese Publikation in der
Deutschen Nationalbibliografie; detaillierte Bibliografische Daten
sind im Internet über http://dnb.d-nb.de abrufbar.

Herausgeber und Vertrieb: Forschungszentrum Jülich GmbH
Zentralbibliothek, Verlag
52425 Jülich
Tel.: +49 2461 61-5368
Fax: +49 2461 61-6103
zb-publikation@fz-juelich.de
www.fz-juelich.de/zb

Umschlaggestaltung: Grafische Medien, Forschungszentrum Jülich GmbH

Druck: Grafische Medien, Forschungszentrum Jülich GmbH

Schriften des Forschungszentrums Jülich
Reihe Schlüsseltechnologien / Key Technologies, Band / Volume 216

D 38 (Master Köln, Univ., 2020)

ISSN 1866-1807
ISBN 978-3-95806-464-5

Vollständig frei verfügbar über das Publikationsportal des Forschungszentrums Jülich (JuSER)
unter www.fz-juelich.de/zb/openaccess.

Abstract

Surface acoustic wave sensors are highly sensitive micro acoustic devices which can be used as microactuators or detectors. In this work a mass detector based on surface acoustic waves has been developed which is suitable for the detection of molecules. The detector is based on a kind of delay line and mainly measures smallest changes of its resonance frequency, which is caused by the mass of molecules adsorbed on the delay line.

Using the conventional piezoelectric material $LiNbO_3$ (Y cut, Z propagation direction) a resolution of the optimized mass detector has been achieved which is equivalent to a thickness resolution of a 3-aminopropyltriethoxysilan (APTES) layer of 0.01 nm. This has been achieved by optimizing the sample holder, sample design and sample mounting and by investigating and comparing their electronic properties via open and short tests. Furthermore our standard lift-off process for the electrode fabrication has been improved by an additional plasma ashing which led to a removal of residual contamination (most likely PMMA) underneath the electrodes and improved the mechanical adhesion.

In order to further enhance the mass detectors' resolution, the mass load sensitivity of epitaxial grown thin film $K_{0.7}Na_{0.3}NbO_3$ (Z propagation direction) on SmScO3 (110 cut) has been investigated and compared to the conventional $LiNbO_3$ bulk material. At the same operating frequency both materials' sensitivities seem to be identical. At low mass loads a linear frequency dependent regime has been observed with the sensitivity of c_m= 0.11 m^2/(MHz kg). This is in agreement with the literature for $LiNbO_3$. At higher mass loads and/or frequencies a deviation of the linearity is observed which leads to a significantly increased sensitivity (factor 9). This regime might not only be of interest due to its higher sensitivity, it could also offer the possibility to use the sensor in liquids by transforming the Rayleigh-type sensor into a Love-type surface acoustic wave (SAW) via adding a wave guiding layer to generate so called Love waves. In addition, the SAW intensity distribution of the various harmonics showed that thin film KNNO seems to be applicable at higher frequencies which would lead to a further improvement in sensitivity.

An attempt has been made to in situ monitor our molecular deposition and removal process of APTES with the developed SAW mass detector. The change of the detectors resonance frequency can monitor both processes. After the deposition the layer thickness of APTES has been determined to 0.35 nm assuming a molecular density equivalent to the liquid state. The frequency recording of the detector shows additional features when opening and closing the molecular source, which could provide further insights into the underlying physics of the deposition process itself.

In conclusion, the optimized SAW mass detector is suitable for molecular detection, and its thickness resolution of 0.01 nm (with respect to the liquid state of APTES) could most likely be improved by thin film KNNO and/or by adding an wave guiding layer on the detector, which could also make it suitable for detection in liquids.

Table of Contents

Chapter 1: Introduction

The market of SAW devices is growing rapidly due to their versatility and thus due to their use in various industries. These are mainly aerospace, defense, telecommunication, automotive or consumer electronics. Especially the increasing demands of the latter like smartphones fuels the growth even more. Apart from this, bioengineering might become a strong contributing industry in the next years as well.

Today we are facing a revolution in new body implantations that can change our understanding of the human physiology and might change our perception of the environment. The smartphone is a technical device which is already indispensable for one or the other and is always close to the body. With the now available cameras, it offers at full zoom even insights into objects that are barely visible to the naked eye, so to speak it expands our sense of seeing and thus it can enhance our perception. Nevertheless, the smartphone can be put aside at any time. So despite the opinion of some people, it is not part of our body and surely it is no implant, no matter what curious videos you find on the internet. However, research is making further progress in the field of bioelectronics, which might enable at some point the cellular phone to be directly coupled to the brain cells. But it is not only the utopian aim of an eye-implant that motivates scientists, it reaches also to devices of the senses of hearing, smelling, feeling and tasting which might be realized to couple to the human brain by bioelectronic technologies.

So these novel implants should therefore communicate directly with the neurons or cells of the body or brain. One major challenge, however, is the development of interfaces that offer perfect electronic properties on the one hand and a viable environment for biological objects on the other hand. In addition to numerous other applications in the field of bioelectronics such as biosensors or actuators, SAW devices can be extremely helpful in the development of these interfaces. A typical technique is making use of linker molecules that couple the inorganic electronics to the receptor or bio object.

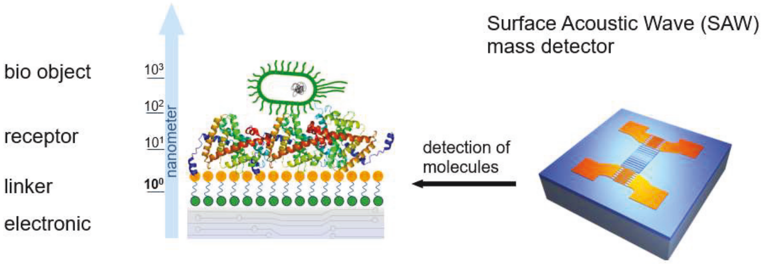

In this work, we try to develop a mass detector that allows in situ monitoring of molecules. This sensor is tested on our molecular layer deposition. As such it not only demonstrates that it is possible to monitor the adsorption of molecules, it might also give further insight to our deposition process and thus improve the quality of our fabricated self-assembled monolayers of molecules. The basic idea is to make use of epitaxial thin films of $K_xNa_{1-x}NbO_3$ (KNNO) as piezoelectric substrates, which are extremely promising candidates for applications in bioelectronics and medicine due to their high piezoelectric properties, their biocompatibility and their possible use at high operating frequencies. The detection of molecules is demanding, but realizing such a device, might enable even further opportunities in the detection of biological matter or bio actuator applications. Following this introduction, this thesis is subdivided into the chapters listed below:

Chapter 2 provides a brief theoretical introduction to the generation, detection and the influence of a mass load to surface acoustic waves.

Chapter 3 includes the present experimental methods for thin film preparation and SAW measurements. Furthermore the quality of fabricated electrodes via our standard lift-off process has been investigated and finally optimized.

Chapter 4 shows the experimental work involved in the development of the SAW sensor. This is substantiated by various electronic tests outside and inside the molecular layer deposition (MLD) chamber.

Chapter 5 comprises the experimental results. It starts with a detailed comparison of the mass load sensitivity of SAW sensors made from KNNO thin films and conventionally used $LiNbO_3$ bulk material. These results are then used to calibrate our sensor. Finally a first successful attempt to in situ monitor a molecular deposition is shown and discussed.

Chapter 6 summarises the results achieved in this work. Furthermore it provides a brief outlook.

Chapter 2: Theoretical Background

In this chapter the basic theoretical knowledge is imparted, which is necessary for the understanding of the practical work and its results. This includes the functional principle of the SAW based mass detection and the necessary physics behind it. The generation of SAWs and their properties are well explained in several textbooks. Mostly based on *Acoustic wave sensors: Theory, Design and Physio-Chemical Applications* [1], the important basics for this work are explained in the following.

2.1 GENERATION OF SAW

A SAW can be directly generated on a piezoelectric crystal, by using a spatially periodic interdigital pattern of electrodes [2]. Since they convert electrical into mechanical energy or vice versa, they are also called interdigital transducer (IDT). Applying a voltage on these IDTs causes a periodic electric potential in the crystal, resulting in a periodic electric field with a periodicity of λ (Figure 1 (a)). Due to the piezoelectric effect, a periodic strain field occurs. Alternating that voltage produces a SAW with wavelength λ. At the IDTs it is a standing wave, however it is propagating away from it in both directions (bi-directional IDT). The propagation direction is perpendicular to the fingers of the IDT. The resulting SAW are also called *Rayleigh waves* and characterized by its elliptical particle motions and their very small penetration depth into the substrate (of the order of λ (Figure 1 (b), (c)).

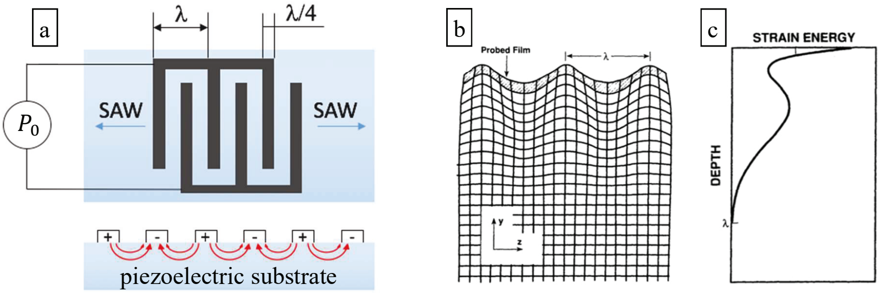

Figure 1: Generation of SAW: IDT on piezoelectric substrate (topview and sideview). The electric field inside the substrate causes a mechanical strain field (b). The resulting SAW (or Rayleigh wave) is propagating in both directions whereas the energy is confined close to the surface (c). (b) and (c) taken from [1].

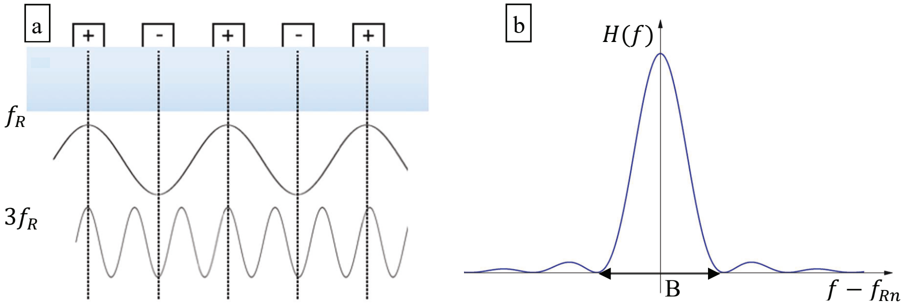

Figure 2: Coincidence of wavelength and IDT period at multiples of the resonance frequency

The transducers efficiency is frequency dependent. It works most efficient at a generator frequency $f_R = v/\lambda$, where v is the SAW propagation velocity. Figure 2 (a) demonstrates, that the SAW mode can only be excited at odd multiples of f_R. The nth harmonic of f_R is given by:

$$f_{Rn} = nf_R = n\frac{v}{\lambda} \tag{1}$$

Near f_{Rn}, the IDTs' amplitude response $H(f)$ is more complex (Figure 2 (b)) and obeys

$$H(f) \sim k\left|\frac{\sin(X(f))}{X(f)}\right| \qquad \text{with} \qquad X(f) = \frac{N\,\pi\,(f - f_R)}{f_R}, \tag{2}$$

N and k are the number of finger pairs within an IDT and the electro-mechanical coupling constant, respectively [3]. The corresponding bandwidth *B* is given by

$$B = \frac{2f_{R1}}{N} \tag{3}$$

and thus inversely proportional to *N*.

2.2 DELAY LINE

The basis of the SAW mass detector is a kind of delay line. It consists of a pair of IDTs with a centre-to-centre distance *D*. One of these IDTs is generating the SAW (generator), whereas the other one is receiving it (receiver) (Figure 3).

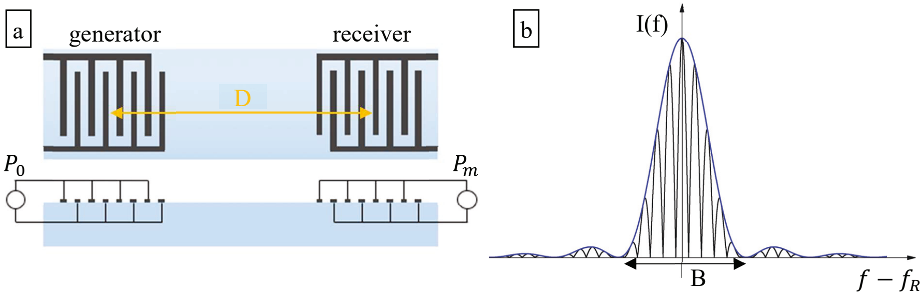

Figure 3: (a) Delay line consisting of two rectangular IDTs. One is operating as SAW generator, the other one as a receiver. (b) Frequency response: intensity of the electrical (blue) and additionally the acoustic (black) transducer's response.

Due to the bi-directional IDTs the insertion loss is at least - 6dB [3], [4]. The received intensity is composed of the SAW with the IDTs' amplitude response $H(f)$ (the intensity is proportional to the square of $H(f)$) and the direct electromagnetic transmission between generator IDT and receiver IDT, propagating with the speed of light. Neglecting the direct transmission (background), the resulting interference (also called beat) is periodic (so-called beating frequency f_b) (Figure 3 (b)). Since the SAWs' velocity is 10^4 times smaller compared to the speed of light, f_b is given by

$$f_b \approx \frac{v}{D}. \tag{4}$$

In principle, the delay line is used to determine the speed of SAWs. Measuring the frequency dependent intensity at the receiver offers finally two possibilities to identify it:

(i) **maximum of the intensity**: identifying the maximum of the intensity and considering the characteristic behavior of the frequency response leads to the SAW velocity $v = f_R\lambda$, where λ is known due to the IDT period.

$$v = f_R\lambda \tag{5}$$

(ii) **beating frequency**: the period $f_b = v/D$ of the interference pattern depends on the SAWs' velocity, as well as on the length D of the delay line. At a given length D the velocity can be determined according to

$$v \approx f_b D. \tag{6}$$

2.3 FRESNEL AND FRAUNHOFER REGIONS IN SAW DEVICES

There are several reasons for an attenuation of SAWs during its propagation through the crystal lattice, through which the SAW energy is dissipated for instance due to heat, acousto-electric losses or crystal imperfection [3]. In addition, diffraction of SAWs may lead to a seemingly attenuation at the receiver. For example by passing through an *acoustic aperture* (finger length of IDTs) the wavefront spreads and does partially not intercept the receiving IDT, resulting in a decreased intensity.

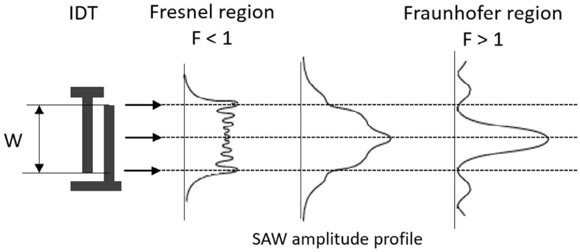

Figure 4: Diffraction of SAWs, Fresnel and Fraunhofer regions and their amplitude profiles.

Therefore, it is always desirable to design the delay line in such a way that the wavefront has a SAW amplitude profile within the Fresnel region when it reaches the receiver (Figure 4). Related to the diffraction equation of classical optics and considering the anisotropy of piezoelectric materials, the diffraction parameter can be approximated by

$$F = \frac{4\lambda D(1 - 2A)}{W^2}, \tag{7}$$

where W represents the IDTs finger length and A is a propagation direction- and material dependent constant [3]. For $F < 1$ the device operates in the Fresnel regime, whereas for $F > 1$ the Fraunhofer regime is present. The so-called anisotropy parameter A is for instance positive for $LiNbO_3$ (YZ) (Y-Cut, Z propagation direction), which means that the near field region is even enlarged compared to the isotropic case. Thus, $LiNbO_3$ (YZ) enables long distance SAW propagation (up to 45 cm) with only small diffraction losses [5].

It is important not to confuse the diffraction pattern with the IDTs response. Diffraction is inverse proportional to the frequency, but if at all it only leads to a slight attenuation of the transducers' response.

2.4 SAW MASS DETECTOR

Based on acoustic waves, there are several types of sensors like the thickness shear mode resonator (e.g. quartz crystal microbalance), the flexural plate wave device or the SAW device. The benefit of SAWs in sensor applications is due to its high energy confinement (2.1), which causes an extreme sensitivity to surface perturbations [1].

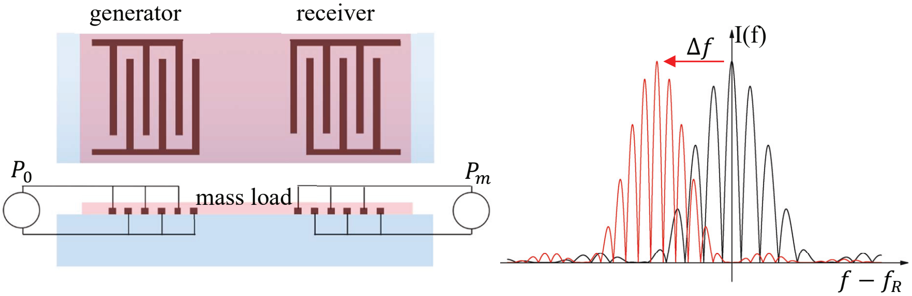

Figure 5: Principle of the SAW mass detector. A mass load on the delay line causes a shift of f_{Rn} and a change of the beating frequency as well.

Acoustic waves are sensitive to several perturbations, such as pressure, strain, humidity or temperature. From energy considerations one can derive the influence of a mass load on the SAW velocity v or the resonance frequency f_R. The basic idea is, that a rigid and very thin layer (less than 1% of the wavelength [6]) with mass density ρ on top of the substrates surface moves synchronously with the SAW. Assuming no attenuation and dissipation of energy, the kinetic energy density increases, due to the additional mass. Since the power density P (power/unit area) does not change, the SAW velocity has to decrease. This results in a relative frequency and velocity change of:

$$\frac{\Delta f_R}{f_R} = \frac{\Delta f_b}{f_b} = \frac{\Delta v}{v} = -c_m f_R \rho \Delta h, \tag{8}$$

where c_m is a material constant which depends only on the substrate material and the SAW propagation direction [1]:

$$c_m = \frac{\pi v_o}{2}\left(\frac{v_{x0}^2}{\omega P} + \frac{v_{y0}^2}{\omega P} + \frac{v_{z0}^2}{\omega P}\right). \tag{9}$$

v_o is the free particle SAW velocity and the terms $v_{i0}^2/\omega P$ are therefore the normalized surface particle velocities of direction i. For many of commonly used piezoelectric substrates, these values have been tabulated by B. A. Auld [7]. Equation (*8*) shows that the relative velocity change Δv scales linear with f_R. Consequently, going to higher operating frequencies enables higher sensitivity. The reason for this behaviour lies in the frequency dependent penetration depth (Figure 1). Higher operating frequency means higher energy confinement. This explains the huge advantage of SAW sensors compared to bulk acoustic wave (BAW) sensors and in particular the commonly used quartz crystal microbalance (QCM). To reach high operating frequencies, very thin and thus fragile crystals are necessary. Hence, the sensors sensitivity depends on

(i) IDT design, especially the period λ
(ii) order of resonance n
(iii) thickness of the resonator

However, the validity of equation (*8*) is limited because of different reasons. One reason is an upcoming difference of group and phase velocity of SAWs caused by the deposited layer. A non-linearity occurs, which has been theoretically investigated [7] and will be discussed later in chapter 5.1.

Chapter 3: Experimental methods

The current experimental basics and methods are described in this chapter starting with the preparation of KNNO thin films (3.1) and followed by the fabrication of electrodes (IDTs for SAW measurement but also IDEs for ferroelectric characterisation). A good quality of the electrodes is the basis for a good sensor, so the standard lift-off process has been evaluated and optimized (3.2). The fabricated samples are now ready for investigation. The present SAW setups and devices are demonstrated (3.3). Finally our home-made molecular deposition chamber is presented in which the molecular depositions, which we would like to in situ monitor, are performed (3.4).

3.1 SAMPLE PREPARATION

The investigated oxide films were prepared with different techniques, namely Pulsed Laser Deposition (PLD) and Metal-Organic Chemical Vapour Deposition (MOCVD). This has been done at Leibniz Institut für Kristallzüchtung (IKZ) in Berlin. Both techniques of epitaxial film growth are briefly explained and their results regarding their quality are demonstrated (3.1.1 and 3.1.2).

3.1.1 Pulsed laser deposition

Pulsed laser deposition is a very versatile process for thin film fabrication. In principle, amorphous, polycrystalline and epitaxial films can be prepared. It is an evaporation technology based on a high power pulsed laser beam.

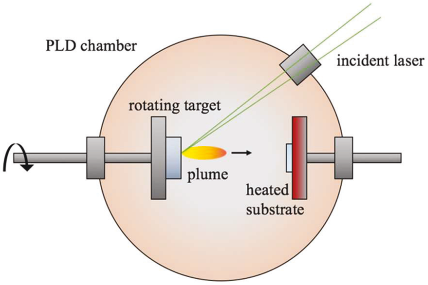

Figure 6: Schematic sketch of the PLD device. Further information is given in the text.

The working principle is shown in Figure 6. A laser beam is focused on the target. The target absorbs its energy and is locally very strongly heated. Material is evaporated and removed from the target (ablation). This material expands to the surrounding vacuum in form of a plasma plum and is deposited on the heated substrate.

Main advantages of this technique is its versatility due to the flexible parameter choice of laser pulse frequency, laser power, background pressure, target, and substrate temperature which makes it a perfect technique for research. However, there are fundamental disadvantages with respect to other techniques like MOCVD. Agglomeration on the substrate can occur, and high energetic particles bombarding the substrate cause usually more crystallographic defects in PLD films.

For this work, various epitaxial films of $(K_xNa_{1-x})NbO_3$ have been prepared, ranging from x = 0.1 up to x= 0.9. These are deposited on single crystal substrates of DyScO3 (110), TbScO3 (110) and GdScO3 (110). A complete list is available in the appendix (page 60). In addition to the substrate and the stoichiometry, the layer thicknesses and the vertical lattice parameters, which have been determined by the IKZ using X-ray, are also listed. For the deposition, the laser power was 5 J/cm^2 at a repetition rate of 10 Hz. The process gas was oxygen at a pressure of 1 Pa, and a typical substrate temperature of 700 °C was used to guarantee an epitaxial growth of the oxide film on the substrate.

3.1.2 Metal-organic chemical vapor deposition

Metal-organic chemical vapor deposition (MOCVD) is another process to prepare epitaxial films. It makes use of chemical precursors and bases on complex chemical reactions and therefore requires more experience and basic knowledge. Nevertheless, this method offers two major advantages compared to PLD. On the one hand, it is very well suited for mass production, which is why it is mainly used in the semiconductor industry. On the other hand, film growth takes place close to thermal equilibrium. This allows a film growth of very high quality, namely a low defect density, a low number of oxygen vacancies as well as very smooth surfaces. The working principle of MOCVD is illustrated in Figure 7.

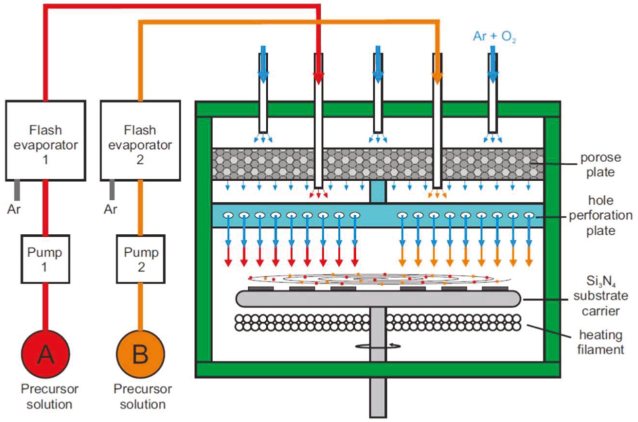

Figure 7: Schematic of the MOCVD device used for this work. Further information is given in the text. Taken from [11] .

In this work, MOCVD was used for the fabrication of a $(K_{0.7}Na_{0.3})NbO_3$ film on a substrate of $SmScO_3$ (110-oriented). K(thd) and Na(thd) ((thd) = 2,2,6,6-tetramethyl-3,5-heptanedione) and $Nb(EtO)_5$, dissolved in dry toluene, are used as source materials for K, Na and Nb, respectively. A homogeneous gas mixture is very important for best results. This is achieved at a pressure of 2.6 mbar, an oxygen to argon ratio of 0.6, a substrate holder temperature of 700 °C and a substrates' carrier rotation speed of 750 rounds per minute.

In order to measure SAWs and permittivity, finally electrodes have to be fabricated on top of the samples, which is described in the following.

3.2 ELECTRODE FABRICATION

The quality of the electrodes is vital for SAW experiments in this work. The electrode fabrication for all samples, $LiNbO_3$ and KNNO thin films (see Table 5 and Table 7), was done via lift-off technique. Its process parameters stem from the fabrication of SiO_2 terminated Si substrates. For this material, the parameters are well established. Since $LiNbO_3$ is less conductive, the process needed to be adapted. The quality of this adapted standard lift-off process is investigated in 3.2.1.

As a part of a further development process, the HNF recently changed the e-beam setup and increased the electron energy of the e-beam lithography from 50 keV to 100 keV. Obviously the e-beam dose had to be adjusted correspondingly. A detailed dose test is presented in 3.2.2. Furthermore, since it turned out that the standard lift-off process needed to be optimized for our SAW experiments (the SAW signal quality directly depends on the quality of the IDTs), an attempt has been made to improve the standard lift-off process by an additional plasma ashing step. Together with the dose test, these results of the *optimized lift-off process* are presented.

An explanation of the standard lift-off process is demonstrated together with the optimizations and its recommended parameters in 3.2.3 (*optimized lift-off process).*

3.2.1 Standard lift-off process

The quality of the standard lift-off process is demonstrated for a $LiNbO_3$ substrate in Figure 8. According to the design, the sample contains different structures, including IDTs and IDEs.

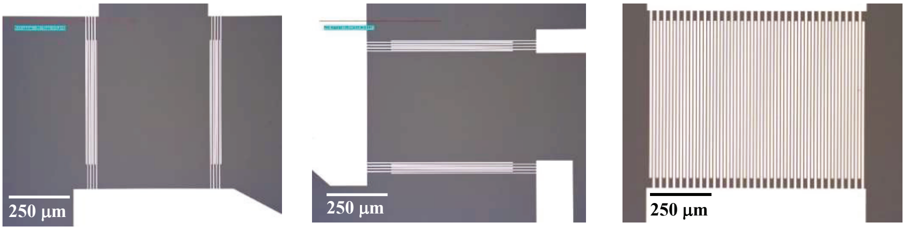

Figure 8: Various electrode structures on a $LiNbO_3$ substrate obtained via the standard lift-off process

The reflected light of the optical microscope illuminates the electrodes brightly. As far as it can be observed, the metal electrodes seem to adhere on the surface. The patterns are well visible and there are no short cuts between fingers for both structures. The surface is very clean and there is almost no contamination.

However first, the individual fingers of the IDEs are designed with a width of 10.0 µm. In the SEM they turn out to have a width of 10.4 µm (Figure 9). The gap between the electrodes thus decreases by 8 % from 5 mm to 4.6 mm. This has a significant impact on the capacitance of IDEs and on the SAW signal of IDTs.

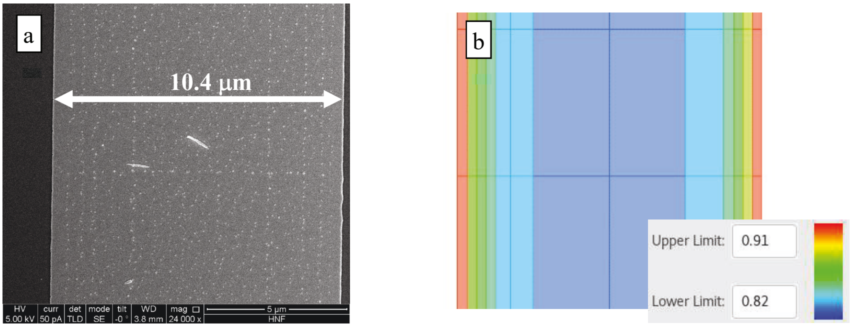

Figure 9:(a) SEM image of an electrode finger of an IDE on $LiNbO_3$. (b) Subfields of the e-beam writing of the electrode shown in a). The colour scale in b) represents the factor of the different e-beam doses with respect to the original dose.

Second, the surface of the electrode shows a contamination pattern of white dots (Figure 9 (a)). This pattern is not visible next to the electrode on the sample surface itself. Since the last step of the electrode fabrication is a careful cleaning, there might be a pollution underneath the electrode. Looking closer to the e-beam lithography, one can find a reasonable explanation:

In order to counteract the so-called *proximity effect*, the electrode pattern is exposed to different electron beam doses (proximity correction). This is done by dividing the electrode pattern into subfields. Within these subfields, the dose is constant, whereas it can differ for different subfields. Comparing the contamination pattern of the electrode with the boundaries of the subfields, a perfect agreement between both patterns can be seen. When scanning a subfield, the electron beam turns at its boundaries. At these turning points, there is supposed to be a deviation of the e-beam dose. As a result, the photoresist seems not to be completely removed after the development. Leftovers of photoresist are still underneath the electrodes. Consequently, the mechanical and electrical coupling is reduced. Since the leftovers are not homogenous, fringing electrical fields will appear. However, it is unclear whether the electrode is at least partially in indirect contact to the sample surface, or whether there is even a thin layer of photoresist left. A thin layer of photoresist would reduce the electrical coupling to the sample even more.

To summarize the results, the standard lift-off process is not fully optimized for our purpose. The electrode width is too large indicating an overdevelopment or too high e-beam dose during lithography, whereas the leftovers of photoresist would ask for larger development or higher e-beam dose. Since the SAW and capacitance measurements require perfect electrodes, the lift-off process had to be optimized. This optimization is described in the next section.

3.2.2 Optimization of the lift-off process

According to a rule of thumb, the e-beam dose usually has to be scaled proportionally to the electron energy (see datasheet of the photoresist manufacturer [8]). This means, instead of using an e-beam dose of 300 µC/cm^2, a dose of 600 µC/cm^2 would be suitable when switching from 50 keV to 100 keV. However, as shown in the previous section the standard lift-off process might not be the best approach. Instead, a detailed dose test was performed. Identical test patterns were exposed with 15 different e-beam doses, ranging from 360 µC/cm^2 to 640 µC/cm^2 (Figure 10).

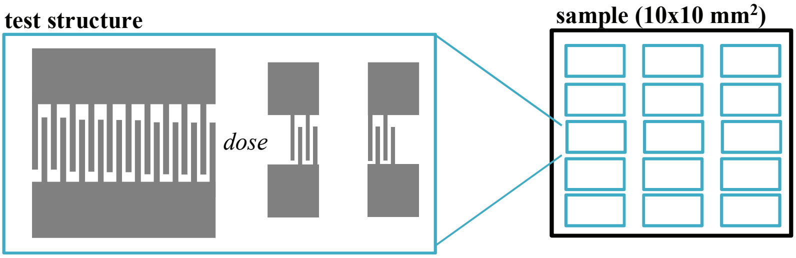

Figure 10: Principle of the dose test: A given test structure, consisting of an IDE and 2 IDTs, is fabricated 15 times on a $LiNbO_3$ substrate. Each of the structure is written by a different e-beam dose ranging from 360 µC/cm^2 to 640 µC/cm^2.

In addition to this test, a further attempt is made to remove the residuals of the photoresist with plasma ashing which was introduced after the development step (see section 3.2.3). The plasma ashing was done with the Gigabatch 310M using an oxygen flow of 200 sccm, a power of 300 W, an exposure time of 390 s and a metallic cage to screen the ions. In order to be able to distinguish the influence of this additional ashing, the dose test was performed on two samples. One sample was exposed to the oxygen plasma, the other one was not.

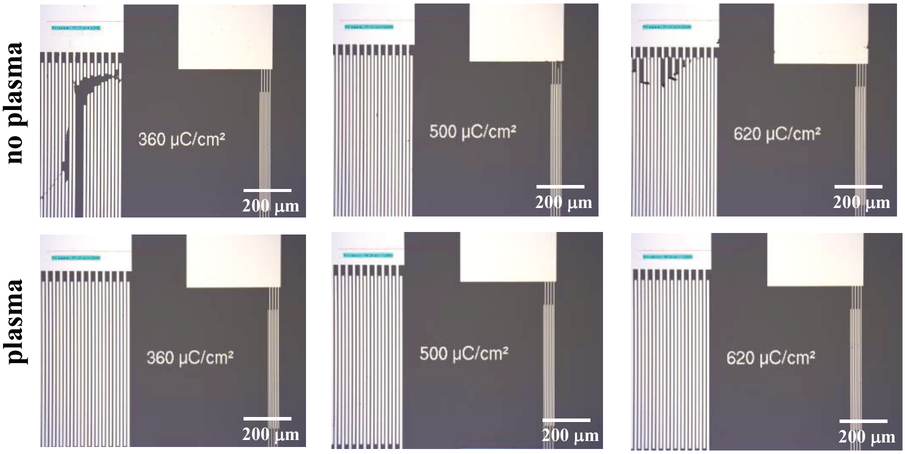

Figure 11: Optical images of typical IDE and IDT structures obtained for different e-beam doses (dose given in the images) for the modified lift-off process without (top) and with (bottom) additional plasma ashing step.

Exemplary the structures of three different e-beam doses without and with additional plasma ashing are shown in Figure 11. The optical microscope reveals a huge impact of the plasma treatment. Within large areas, the electrodes seem to adhere to the surface in both cases (with and without plasma treatment). However, the single electrodes of the plane capacitor indicate that there is an adhesion problem. In particular, one can see clearly a peeling off of the electrodes at an e-beam dose of 360 µC/cm^2 and 620 µC/cm^2. For the plasma treated sample, all electrodes, independent of their size, seem to adhere on the surface very well. Furthermore no shortcuts between the fingers are visible (Figure 11).

Also the SEM shows major differences between both samples (Figure 12). The sample without plasma treatment, shows still leftovers of photoresist underneath the electrodes. It seems that the amount of impurities reduces for higher e-beam doses. Thus, the electric coupling to the substrate might be reduced. The edges of the electrodes seem to be heavily contaminated and a slight peeling off of the edges is visible. However, the plasma treated sample does not show these regular impurities (for none of the e-beam doses) and the edges of the electrodes do not peel off and are very precise. Even the lift-off seems to have worked better. Consequently, adding the plasma ashing process after the development of the photoresist, leads to much better quality of the electrodes. Firstly, the electronic coupling of the electrodes will be better, and secondly, the success rate is significantly higher.

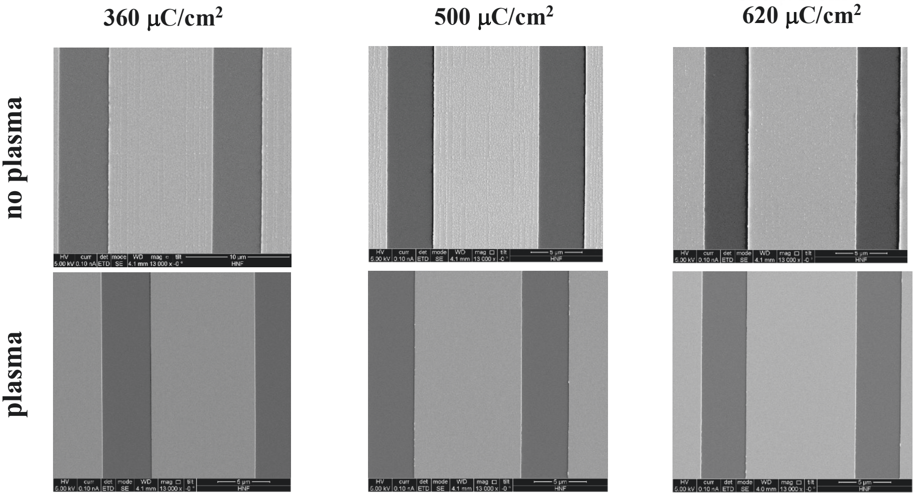

Figure 12: SEM images of the IDE structures shown in Figure 10 for the modified lift-off process without (top) and with (bottom) plasma ashing.

At a first glance, there is no difference between different e-beam doses after the plasma treatment. However, the electrode width depends strongly on the e-beam dose. Both, the electrode width of the IDEs (designed to be 10 µm) and the electrode width of the SAW IDTs (designed to be 3 µm) have been analyzed. This is demonstrated in Figure 13. At first sight, it looks like the width of both fingers is increasing linear with the e-beam dose. Extrapolating these linear dependence, the optimum e-beam dose of the plasma treated sample should be at 355 µC/cm^2 for IDEs and 240 µC/cm^2 for the IDTs. This means at these e-beam doses the width would exactly match the design. But a closer look indicates a saturation of the width below an e-beam dose of 400 µC/cm². At this e-beam dose the deviation to the originally designed width (blue line) is already quite small. It is smaller than 100 nm for the fingers of the IDEs and smaller

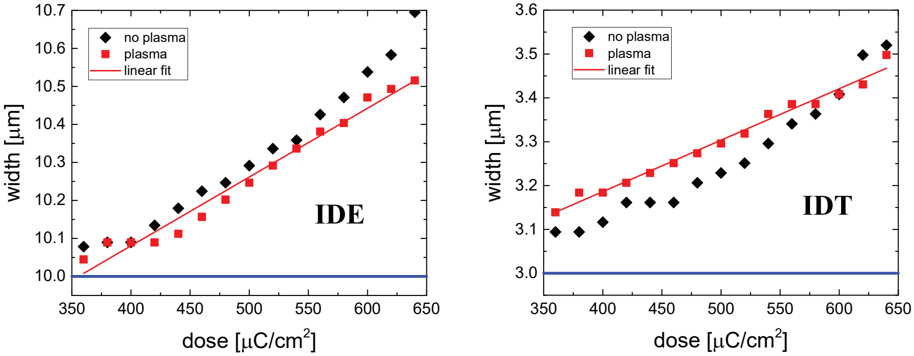

Figure 13: Widths of the fingers of the IDE (left) and the IDT (right), without plasma treatment (black) and with plasma treatment (red). The data is derived from SEM images. The blue line indicates the originally designed width.

In conclusion, plasma ashing causes a significant improvement of electrode fabrication of the IDEs and IDTs on $LiNbO_3$. The success rate of the fabrication seems to be significantly higher and even more important, the residual photoresist is removed. The electric coupling, as well as the adhesion of the electrodes on the surface is better. Measuring the electrode width for different e-beam doses, shows that at e-beam doses of 360 µC/cm² to 400 µC/cm² only small deviations of less than 200 nm occur.

3.2.3 Optimized lift-off process

The basic idea of this technique is to first create a negative mask of the structure consisting of a sacrificial layer on top of the sample (steps 1 to 6b). After that, a metal layer is deposited (step 7) and finally the sacrificial layer is removed together with the sacrificial layer on it (step 8). Steps 3 and 5 are those added to the process used for SiO_2 terminated Si. Step 6 (b) and the parameters for the e-beam lithography (marked in bold) are recommended due to the previous optimization.

Regarding the fabrication it is very important to work in a clean and particle free atmosphere. Therefore, the following steps have been performed in the cleanroom of the Helmholtz Nano Facility (HNF), which provides different working areas fulfilling the DIN EN ISO 14644 with classes ISO 1 – 3.

1. *Chemical cleaning*

- cleaning in acetone (5 minutes) and 2-propanol (5 minutes) in an ultrasonic bath at 100% (320W), 37 kHz and room temperature
- drying with nitrogen gas

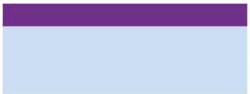

2. *Photoresist coating*

- spin-coating the photo resist poly(methyl methacrylate) PMMA 669.07 600K (Allresist): 5 s at 1000 rpm followed by 55 s at 4000 rpm
- annealing on a hot plate at 140 °C for 15 min, resulting in a layer of 800 nm thickness

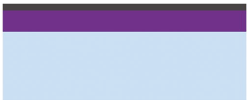

3. *Chrome deposition*

- evaporation deposition of 10 nm chrome using Balzers PLS 500

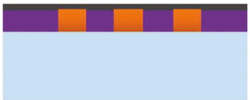

4. *E-beam lithography*

- photoresist is exposed to an electron beam (VISTEC EBPG 5000 plus) according to the pattern with an electron energy of **100 keV** and an e-beam dose of **400 $\mu C/cm^2$** (standard process: energy 100 keV, e-beam dose 400 $\mu C/cm^2$)

5. *Chrome etching*
- etching with a mixture of ceric ammonium nitrate ($(NH_4)_2[Ce(NO_3)_6]$), perchloric acid ($HClO_4$) and deionized water mixed at a ratio of 10.9 : 4.25 : 84.85 (MicroChemicals), for 12 s
- rinsing in deionized water for 30 s
- drying with nitrogen gas

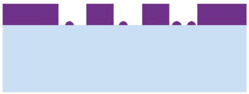

6. *(a) Development*
- removing the exposed photoresist by methyl-isobutyl-ketone AR-600-55 (Allresist) for 90 s
- rinsing with 2-propanol for 1 min
- drying with nitrogen gas
- ⇛ negative mask on top of the sample is ready

6. *(b) Plasma ashing*
- removing of the remaining photoresist using Gigabatch 310M with a metallic cage, a power of 300 W, an oxygen flow of 200 sccm and an exposure time of 390 s

7. *Electrode deposition*
- evaporation deposition of 5 nm titan and 45 nm platin using Balzers PLS 500

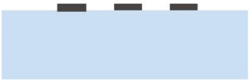

8. *Lift-off*
- removing the sacrificial layer with acetone for 15 min in an ultrasonic bath at 100% (320W), 37 kHz and room temperature
- cleaning with 2-propanol
- drying with nitrogen gas

3.3 PRESENT SAW TECHNIQUES

In this section the experimental SAW setup, the standard IDT design and sample holder, as well as important measurement parameters are presented (3.3.1). In addition, it is demonstrated how the beating frequency and resonance frequency are derived from the measured data (3.3.2).

3.3.1 SAW setup

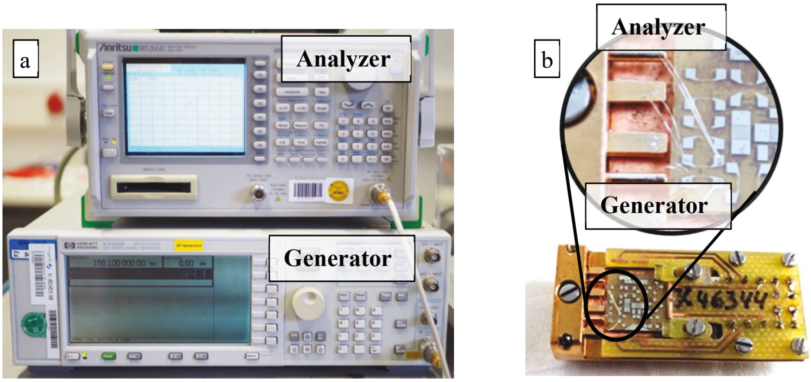

Figure 14: SAW devices; high-frequency generator and spectrum analyser (a), standard sample holder with bonded sample (b).

SAWs are investigated with the help of a transmission setup (2.2). Frequency dependent measurements of the transmission coefficient S_{21} are performed, using a high-frequency generator (Hewlett Packard, E4422B, ESG series signal generator, 250 kHz - 4.0 GHz) and a spectrum analyzer (Anritsu, MS2661C, 9 kHz - 3 GHz) (Figure 14 (a)). These are connected via high-frequency cables to the sample holder (Figure 14 (b)). Its male SMA plugs are bonded to the sample and finally contacted to the IDTs. All measurements are performed with a power of 1 mW = 0 dBm. Choosing a frequency span at the analyzer of 10 kHz, a video bandwidth filter of 100 Hz and a resolution bandwidth filter of 1 kHz turned out to be a good compromise to minimize measurement time (≈ 1150 ms per point) and noise.

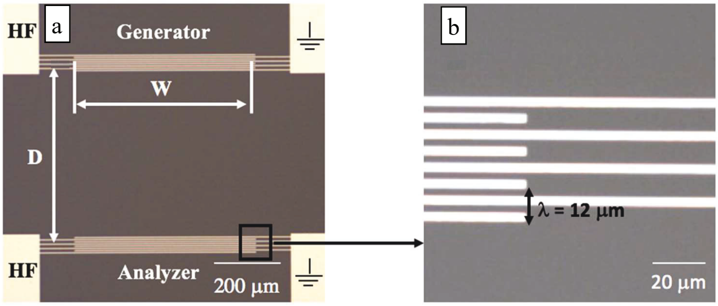

Figure 15: IDT design on LNO; (a) generating and receiving IDTs, (b) close up of the fingers (digits).

Figure 15 shows the IDT structure used in this work which consists of 4 finger pairs. The thickness, as well as the spacing of the fingers is 3 µm, resulting in a period of 12 µm. Hence the SAWs fundamental wavelength is fixed to 12 µm (2.1). These parameters are kept for all measurements in this work. However, the center to center distance D of generating and receiving IDT and the finger length (acoustic aperture) W differ slightly for different designs. In most cases they are 500 µm. For LNO this results in:

(i) a Fresnel parameter F = 0.008 (equation (7)). Therefore, all designs are far in the Fresnel region, no power loss due to a spreading of the SAW front is expected.

(ii) a fundamental resonance frequency f_R= 290.67 MHz (equation (1)).

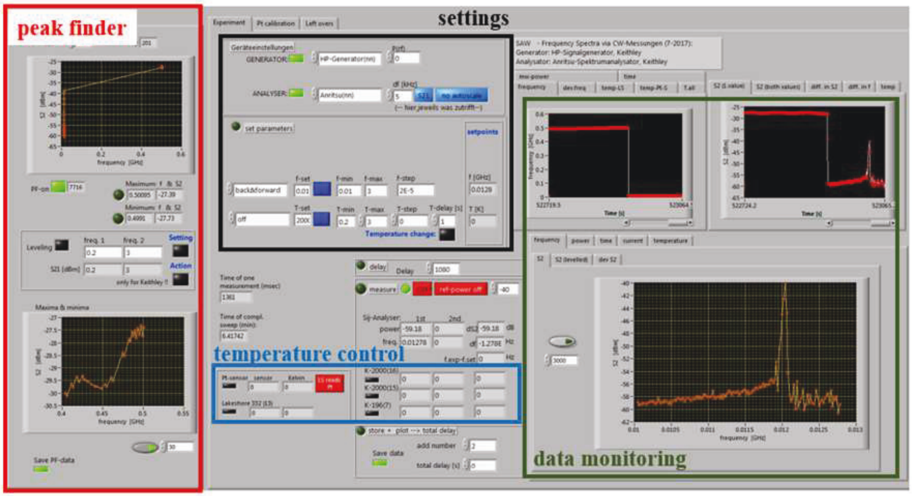

Figure 16: Menu of the home-made Labview control system for the SAW setup.

The hardware is controlled by a computer using a home-made Labview program (Figure 16). The system allows to change all important parameters. Moreover, it is possible to monitor the measurement day and night. Additionally, temperature sensors and a heater can be used for ryogenic measurements. An implemented peak finder simplifies the SAW analysis (see next section).

3.3.2 SAW measurement technique

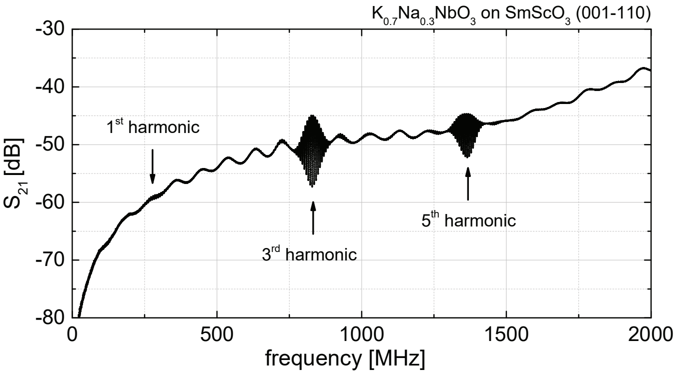

Figure 17: Complete frequency spectrum of S_{21} *for* $K_{0.7}Na_{0.3}NbO_3$ *on* $SmScO_3$ *(110-001) including the 1st, 3rd, and 5th harmonic.*

The recording of a complete frequency spectrum of S_{21} up to a frequency of 2 GHz with a typical step size of 20 kHz takes ≈ 2 days. An example of such an overview spectrum for KNNO on SSO is shown in Figure 17. The capacitive background as well as the interference pattern of 1st (fundamental), 3rd and 5th harmonic of the SAW are well visible. These harmonics offer two options to determine the SAW velocity (2.2), which is simplified by the *peak finder* of the Labview program. The program allows to identify maxima and minima of the interference pattern during the measurement (Figure 18 (a)).

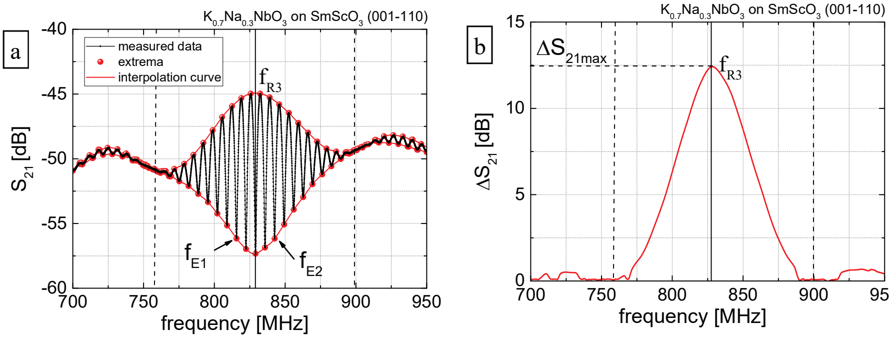

Figure 18: Frequency spectrum of S_{21} *of the third harmonic for* $K_{0.7}Na_{0.3}NbO_3$ *on* $SmScO_3$ *(110-001). The measured data, extrema and interpolation curves (a), and the calculated SAW intensity from the interpolated curves (b) are shown.*

The first method is based on the analysis of the beating frequency. Selecting two extrema f_{E1} and f_{E2} (Figure 18 (a)), the beating frequency f_b is given by:

$$f_b = (f_{E2} - f_{E1})\frac{2}{\Delta n + 1} \tag{10}$$

where Δn is the number of extrema between f_{E1} and f_{E2}. Obviously, the larger Δn, the lower is the uncertainty of f_b. However, away from the center of resonance, first the amplitude of the beating frequency decreases and second the background causes a shift of the automatically analyzed extrema towards the resonance frequency which finally leads to an underestimation of f_b. As a compromise, always two extrema have been selected close to the center of frequency with $\Delta n = 9 \pm 2$. The SAW velocity is finally determined by equation (*6*).

In the second method, the identified extrema are used to determine the frequency dependent SAW intensity ΔS_{21}. Minima and maxima are separately interpolated using Akima spline (red curves, Figure 18 (a)) and subtracted from each other (Figure 18 (b)). Subsequently the difference ΔS_{21} between maxima and minima resembles the expected IDTs frequency response (2.1) which allows to determine the resonance frequency f_{Rn} at the maximum ΔS_{21max} and the bandwidth (dashes lines, calculated with equation (*3*)). The SAW velocity is finally determined by equation (*5*).

Both methods were used to determine the SAW velocity. Based on a measurement on a $LiNbO_3$ substrate (4.2), they will be compared with each other in terms of their accuracy and their correspondence with the literature.

3.4 MOLECULAR DEPOSITION CHAMBER

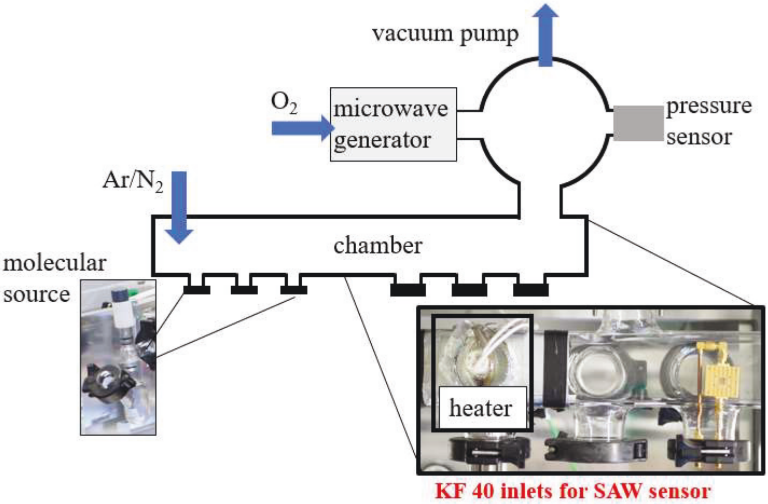

Figure 19: Scheme of the MLD chamber with flange positions for the SAW sensor, sample holder and optical heater.

The home-made chamber for molecular layer deposition (MLD) is shown in Figure 19. At the marked gas supplies it can be filled with nitrogen, argon (carrier gas for MLD) or oxygen (to create ozone with the microwave generator, which is used for cleaning and activating the substrates' surfaces). Two pumps can vacuum the chamber down to 10^{-4} mbar. Additionally, an optical heater, thermocouple and pressure sensor are implemented. In this work, the molecular source is filled with 3-aminpropyl(triethoxysilane (APTES).

Furthermore, there are several KF 40 inlets for installing additional devices or sensors. Since the current SAW device (Figure 14 (b)) cannot be mounted and used inside the chamber, a new holder is developed. The development and testing of the SAW sensor are described in the next chapter.

Chapter 4: Experimental developments of SAW techniques

In order to in situ monitor a molecular deposition it was necessary to develop a SAW setup which enables very precise measurements on the one hand and which is mechanically and chemically robust on the other hand. Furthermore, a measurement methodology is required that allows to measure changes in SAW velocity fast and extremely sensitive.

In this chapter we show

(i) the development of a SAW sensor (4.1).
(ii) a test of the SAW sensor on $LiNbO_3$ (4.2).
(iii) the development of an extremely fast measurement methodology (4.3).
(iv) and first tests of the SAW sensor inside the MLD chamber (4.4).

4.1 DEVELOPMENT OF THE SAW SENSOR

The requirements that the SAW sensor has to fulfil in order to be used in the MLD chamber and to enable very precise measurements are shown in 4.1.1. In order to satisfy these requirements different sample holders, sample designs and sample mountings have been developed. They are presented and compared with each other with respect to their electronic properties (4.1.2 - 4.1.4).

4.1.1 Requirements

Since the current SAW device (Figure 14 (b)) cannot be mounted and used inside the MLD chamber (Figure 19), a new device is developed which has to fulfil many requirements.

Mechanical requirements:

- mountable on a KF 40 vacuum flange with a high frequency cable feed-through
- dimensions limited by the KF 40 inlet and the glass tube of the chamber
- ozone resistant materials and contacts

Electronical requirements:

- low electric losses and no crosstalk between the feed lines and thus high energy transmission through the sample in order to obtain a high intensity of the SAW
- short-term as well as long-term stability of the electronic background in order to have a low noise and a comparability between different measurements
- low background resonances for easier data analysis and avoidance of misinterpretations

Sample design requirements:

- orientation dependent measurement of SAW and capacitance should be possible
- temperature monitoring (especially for capacitance measurements) should be possible

4.1.2 Sample holders

BNC-U

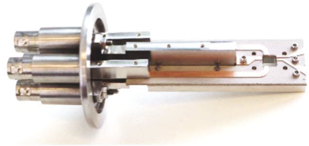

- KF 40 with 4 industrially welded BNC feedthroughs ensure a high vacuum performance inside the chamber.
- Contacts between the circuit board and the BNC conductors is achieved by self-made connectors.
- All parts are screwed and hence dismountable.

SMA-U

- Soldered contacts reduce electric losses.
- The ground plate is instantly mounted on a KF 40 via SMA connectors, whereby the feed lines have to be U-shaped.

SMA-X

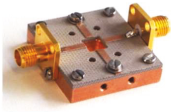

- Soldered contacts reduce electric losses.
- The feed lines on the circuit board are X-shaped, which might show less crosstalk. Therefore semi-rigid high frequency cables are necessary for the mounting inside the chamber.

Up to now the samples had been contacted by bonding to the sample holder. With regard to the application in the MLD chamber, this is now to be replaced by directly pressing the samples onto contacts of a newly developed sample holder. This should enable a better electronically reproducible measuring signal, higher mechanical and electronical stability, as well as a simpler and faster contacting. Therefore, three sample holders, each showing advantages and disadvantages, have been developed and tested. Photos of the sample holders and their most striking features are listed above.

To monitor the molecular deposition, the electronic properties mainly the coupling between input and output (cross talk), electric losses and electric resonances are decisive. The ideal sample holder should show none of these effects. Crosstalk and losses cause a decrease of the power transfer through the device under test (DUT) and result in a decrease of the measuring accuracy. Resonances significantly complicate data analysis and may cause misinterpretations of data. These effects are investigated in the following by open and short test.

Short test

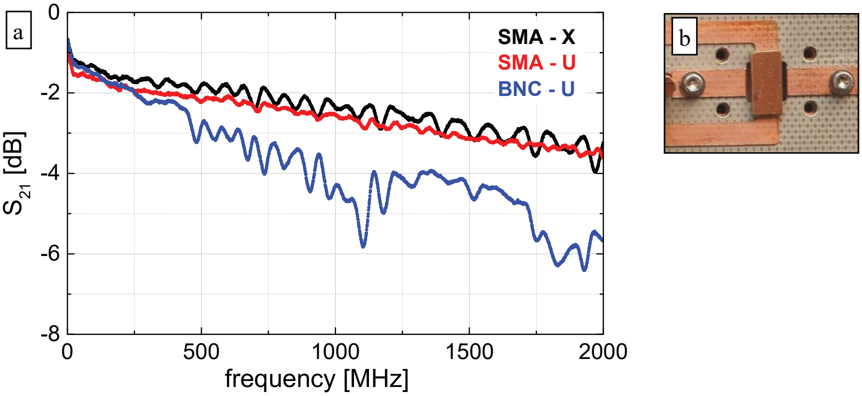

Figure 20: Short test for different sample holder (a) using a windmill design suitable circuit board shorted by a copper bar (b).

The short test is mainly used to determine the electrical losses of a setup. For this purpose the DUT has to be shorted. This has been done with a piece of copper pressed onto the high frequency contacts (Figure 20 (b)). For each sample holder, the transmission coefficient S_{21} decrease with frequency since the inductive impedance plays the major role in a shorted circuit (Figure 20 (a)). The losses of both SMA setups (SMA-X and SMA-U) are comparable (e.g. $S_{21} = -3$ dB $\triangleq$ 0.5 P_0, at f = 2 GHz). However, the transmission coefficient of the BNC-U setup is much worse ($S_{21} = -5.5$ dB $\triangleq$ 0.28 P_0, at f = 2 GHz), resulting in roughly twice the loss of the SMA setups. In good approximation, there should be hardly any impedance changes in the cables, the feed lines on the circuit board and standardized high-frequency connectors (BNC and SMA). Crucial point of the setups are therefore any kind of connections where impedance mismatches lead to reflection of the electromagnetic wave. Candidates are typically the connections from high frequency cable to circuit board and circuit board to sample (here the Cu short). Apparently, the screwed connectors of the BNC-U are significantly worse than the soldered f the SMAs.

Open test

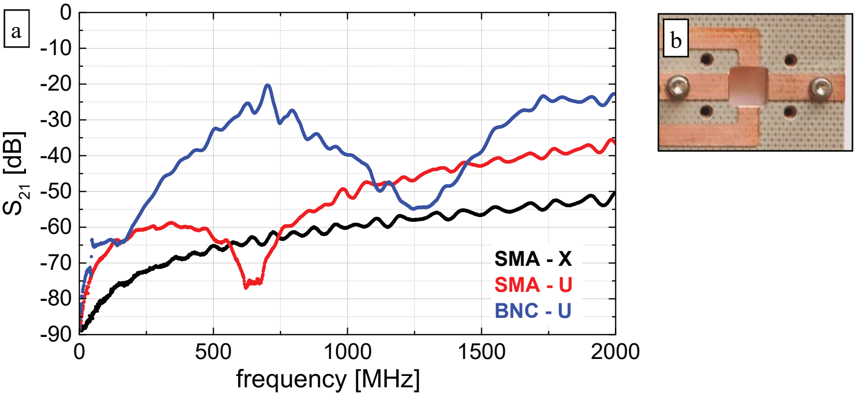

Figure 21: Open test for different sample holder (a), using a windmill design suitable circuit board (b).

The open test is performed to determine the crosstalk. In this test, the frequency spectrum of S_{21} without any sample is measured (Figure 21). Despite small resonances with an amplitude of $\Delta S_{21} \approx 1$ dB, the SMA – X behaves almost like a perfect capacitor. Even at a frequency of 2 GHz its transmission is very small (< -50 dB). In contrast, the SMA-U shows a broad resonance between 500 MHz and 800 MHz and, except for this resonance its transmission parameter is 10 dB to 15 dB higher compared with the SMA-X. The BNC-U has very broad and strong resonances as well (700 MHz and 1700 MHz) and the transmission is much higher compared to the SMAs.

If charges oscillate along a line, it acts like an antenna and radiates EM waves. This holds also for the U-shaped electric lines of the circuit board. The input line acts as transmitting and the output line as a receiving antenna. As the SMA-U with its U-shaped electric lines shows a much higher power transfer between input and output, the grounded shielding between both lines is apparently not efficient.

In summary, the connectors of the BNC-U seem to generate a strong resonance which can make an analysis of measurements difficult. The simple shielding of the setups with U-shaped electric lines does not work efficient and results in a huge crosstalk. Taking both tests (open and short) into account, the SMA-X seems to be the best setup in terms of all features.

4.1.3 Sample designs

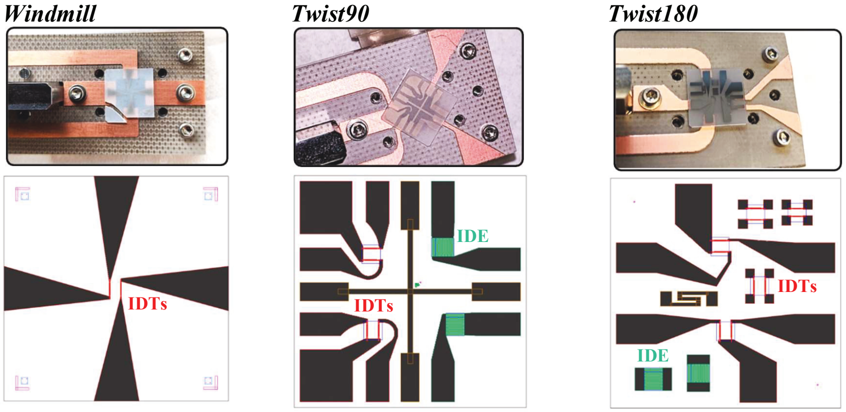

Windmill	Twist90	Twist180
Capacitance: -	Capacitance: 2 directions (bonding)	Capacitance: 2 directions (bonding)
Temperature: -	Temperature: (pressing)	Temperature: (bonding)
SAW: 1 direction (pressing)	SAW: 2 directions (pressing)	SAW: 2 directions (pressing) 2 directions (bonding)

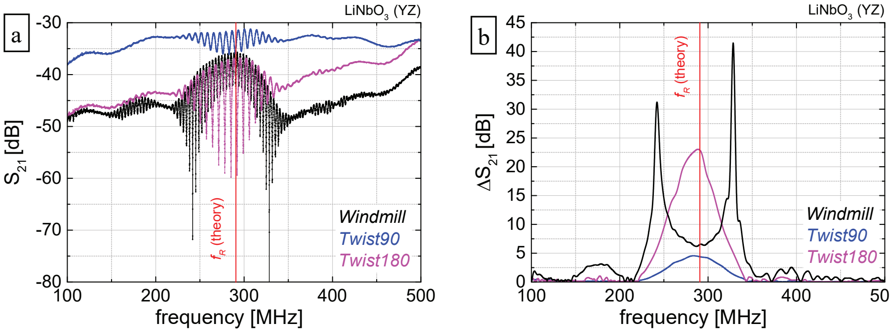

Figure 22: Frequency spectrum of S_{21}. 1st harmonic of $LiNbO_3$ (YZ) with different electrode designs and circuit boards on BNC-U. The red line indicates the expected fundamental resonance frequency f_R, which is calculated from the IDTs' period and the SAW velocity taken from literature [7].

Apart from developing a sample holder, the sample design itself (excluding the IDEs and IDTs) represents another challenge. On the one hand, the design of the feed lines, transferring the electric energy from the contact points of the sample holder to the IDTs/IDEs might have a huge impact on the measurement (due to capacitive coupling). On the other hand, various electrode structures are to be combined on each sample, in order to be able to measure the directional dependence of SAWs and capacitance and, simultaneously, the temperature. For this purpose three different sample designs have been developed and tested. For each of these designs a different circuit board had to be prepared. Due to "historical reasons", these tests has been carried out on the BNC-U setup using $LiNbO_3$ samples. For a better comparison always the Z propagation direction of $LiNbO_3$ has been measured ($LiNbO_3$ (YZ)). However, the distance of the IDTs of the Windmill (1000 μm) and the Twist (500 μm) designs are different. The same holds for the finger lengths. Since the SAW attenuation of $LiNbO_3$ (YZ) is ~ 1.07 dB/cm the latter does not play an important role [3]. Figure 22 shows the 1st harmonic for the three designs in form of the measured raw data (a) and the resulting SAWs' intensity ΔS_{21} (b):

(i) Resonances: Twist180 and Twist90 show the expected transducer response (2.2), although the side lobes are very weak. The Windmill design deviates from this. On the first glance, they look like different diffraction patterns, Fresnel pattern in case of the Windmill design and Fraunhofer pattern in case of the Twist designs. However, this is not the right explanation: The transmission coefficient S_{21} depends on the transducer response. Due to divergence of the SAW, diffraction may cause an attenuated S_{21}. However, both designs are clearly in the Fresnel near-field region (2.3, 3.3.1), which means that this effect is negligible. The enveloping shape of S_{21} of the Windmill design is caused by a strong resonance, which stems from the huge feed lines on the sample. This has been confirmed with further Windmill designs.

(ii) Background: The background signal increases from Windmill via Twist180 to Twist90. With respect to the previous discussion of the resonances, the interpretation might be misleading in case of the Windmill structure again. So it's difficult to make a statement here. However, both Twist designs do not show strong resonances, but a clear difference in the background signal. At f_R they differ by ~ 6 dB, and even more for lower frequencies. In case of Twist90 the feed lines are very close to each other, which may cause increased cross talk.

(iii) Intensity: In terms of intensity, the analysis and comparison of the Windmill structure are difficult (due to the different type of resonances). However, the twist designs show a clear difference in intensity. The maximum intensities differ by about 18 dB (in terms of power this is a factor of 63). The difference is therefore much larger than that of the background. Using the PVC cover it turned out that it is very difficult to mount the sample such that the contact points between sample and circuit board match. Due to the small contacts, this is even more difficult for the Twist90 design.

In summary, the Twist180 design shows a significantly higher SAW intensity at the resonant frequency, no noticeable resonances, and a small crosstalk at the same time. The Twist180 design also includes all necessary IDEs, making it ideal for the investigations of this work.

4.1.4 Sample mountings

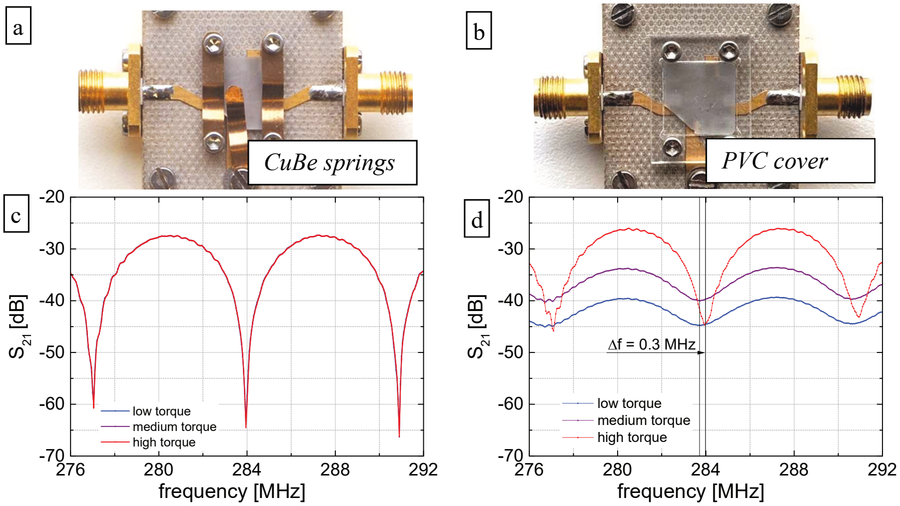

Figure 23: Frequency spectrum of S_{21} of the 1st harmonic on $LiNbO_3$ (YZ). The sample was fixed with copper beryllium springs (all 3 spectra lie on top of each other) (a) and a PVC cover (b).

Last step of the setup engineering was the test of two different contact methods. For this purpose CuBe springs and a PVC cover have been developed (Figure 23). Both, the springs and the PVC cover are fixed with screws. The pressure onto the sample can be adjusted by the torque applied to the screws. To test the mountings, the first harmonic on $LiNbO_3$ (YZ) has been investigated. Therefore, three different torques has been applied. Figure 23 shows a small frequency range of S_{21} at the first harmonic. In case of the CuBe springs, S_{21} shows a very high and torque independent intensity with a $\Delta S_{21} = 37$ dB (Figure 23 (a)). Within the displayed resolution, the measurements are identical. However, with PVC cover, the transmission coefficient depends very much on how the screws are tightened (Figure 23 (b)). From low to medium and finally high torque ΔS_{21} is increasing from 5.4 dB to 6.4 dB and 18.5 dB, respectively. Moreover there is a frequency shift of 0.3 MHz from lower to higher toque. Considering the IDTs parameters, this would correspond to a shift of the SAW velocity by 3.6 m/s.

Using the CuBe springs, the sample can be precisely positioned at the contact areas. This results in a very good connection between sample and circuit board, without change of impedance match between input and output. Using the PVC cover, the sample is pressed on the entire sample backside, whereas the exact pressure points cannot be controlled. The sample might be slightly tilted and the pressure on the three contact areas surely differs. This causes impedance mismatches, resulting in a strong reduction of the intensity, phase shifts and finally a seemingly frequency shift of the spectrum. In addition, due to the fact that LNO is very brittle, numerous samples were broken with the PVC cover due to high tension.

In summary, the CuBe springs provide best properties and are preferable, mainly because of:

(i) reliable, reproducible and comparible contacting
(ii) good contacts, high microwave transfer and thus high intensity of SAWs
(iii) ozone stable and no damage to sample

4.2 TEST OF THE SAW SENSOR

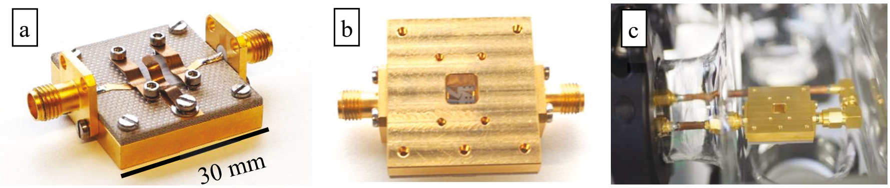

Figure 24: Final developed in situ SAW device SMA-X with a $LiNbO_3$ sample, Twist180g3 design, and CuBe springs. The device and its dimensions in (a), overview from the backside in (b) and mounted inside the MLD chamber in (c).

Based on the information and experience gained from the elaborate sensor development summarized in the previous chapter 4.1, the optimized final sensor was manufactured, consisting of a SMA-X sample holder, a Twist180g3 sample design and CuBe springs (see Figure 24). For electronic long term stability, all contacts have been chemically coated with gold.

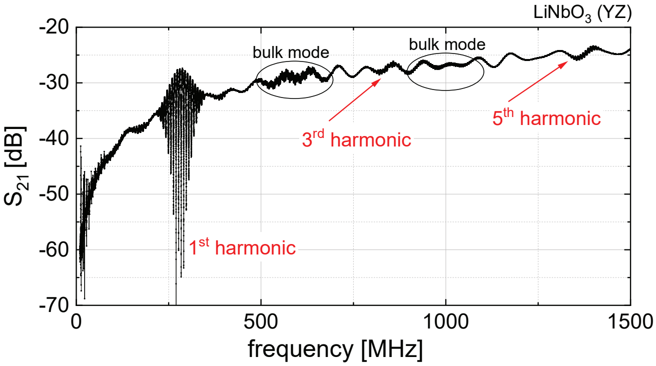

Figure 25: Frequency spectrum of S_{21} for $LiNbO_3$ (YZ) using the developed SMA-X(gold) setup, Twist180g3 design and CuBe springs. The 1st, 3rd and 5th SAW harmonics as well as bulk acoustic waves are marked.

The first test on $LiNbO_3$ (YZ) is shown in Figure 25. It depicts the frequency spectrum of S_{21}, including the 1st, 3rd and 5th harmonics of f_R. Between these harmonics there are contributions of bulk modes as well which are of minor importance here. The device shows an extremely strong SAW intensity of $\Delta S_{21\mathrm{max}} = 42.5$ dB (determined according to 3.3.2) at the first harmonic (Figure 26 (a)). The maximum in S_{21} at f_{R1} is at - 27.5 dB. Considering the losses determined from the short test (- 1.8 dB), the coupling constant ($K^2 = 4.5\% \mathrel{\widehat{=}} \Delta S_{21} =$ - 13.5 dB), the bidirectional IDTs (- 6 dB) and attenuation (- 0.5 dB), in total a maximum intensity in S_{21} of – 21.8 dB is expected [3]. This means by optimizing the sample design (e.g. impedance of IDTs to 50 Ohm), $\Delta S_{21\mathrm{max}}$ could be increased from 42.5 dB to a maximum of 48.7 dB.

The 3rd and 5th harmonics are separately shown in Figure 26 (b) and (c). The theoretical and measured resonance frequencies are added, indicated by red and blue lines, respectively. The 3rd harmonic lies close to a bulk acoustic wave mode which is visible in form of the beating at higher frequencies. Furthermore the intensities of the higher harmonics are smaller than 1 dB. However, their resonances can be determined with an uncertainty of less than 5 MHz which corresponds to an uncertainty of SAW velocity of less than 20 m/s.

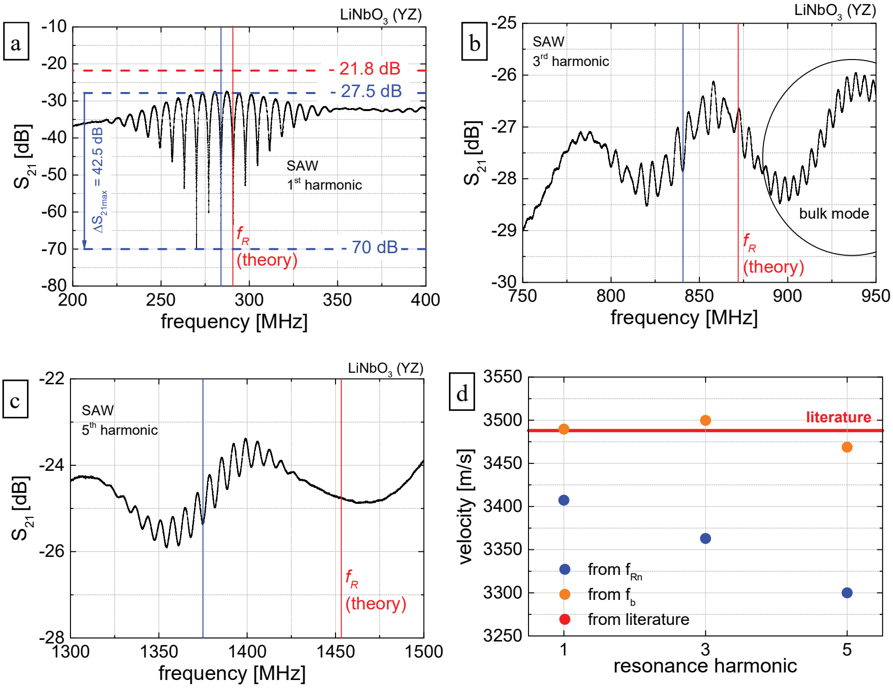

Figure 26: Test of the optimized SMA-X(gold), $LiNbO_3$ (YZ) and Twist180g3 design. S_{21} of 1st, 3rd and 5th harmonic are shown in (a), (b) and (c), respectively. Blue/red solid/dashed lines indicate the measured/theoretical resonance frequency/transmission minima and maxima, respectively. (d) shows the resulting SAW velocities evaluated from the resonances frequencies (orange, equation (5)) and beating frequencies (blue, equation (6)).

The resulting SAW velocities based on f_R (equation (5)) and f_b (equation (6)) have been determined and are illustrated in Figure 26 (d). The velocities determined from f_R seem to be strongly frequency dependent. In contrast, the velocities calculated from f_b are more or less independent from the harmonic and fit very well with the expected free particle surface velocity of 3488 m/s of the literature [7]. Assuming that the resonance frequency depends mostly on the SAW velocity at the location of the IDTs and the beating frequency mostly on the SAW velocity between input and output IDTs, this different behavior is reasonable. Since there is automatically a huge mass load on the substrate caused by the IDTs (metallization ratio 0.5, electrode height 50 nm mainly consisting of Pt with a density of 21.45 kg/m^3), the velocity should decrease according to that mass (2.4). However, between input and output there is no mass load.

As a result, first the developed SAW sensor shows am extremely huge intensity at the first harmonic, which represents a great opportunity for envisioned monitoring of MLD. Second, the beating frequency f_b is much more trustworthy as indication of the SAW velocity compared to the resonance frequency f_R. Thus, the setup is in principle ready for the envisioned molecular detection. Before we demonstrate the SAW sensor in MLD, the sensor algorithm and the implementation of the setup in our MLD chamber are described.

4.3 ALGORITHM FOR THE IN SITU SAW SENSOR

The idea of the algorithm is based on analyzing the change of the beating by tracking a sharp minimum within the interference pattern close to the resonance frequency. For this purpose, a *minimum tracker* has been implemented into the Labview control system (Figure 27) which recognizes smallest changes of the SAW velocity and attenuation of SAWs in less than 2.4 s. In addition, the control of the MLD setup (gas flow, pressure, temperature, etc.) has been implemented.

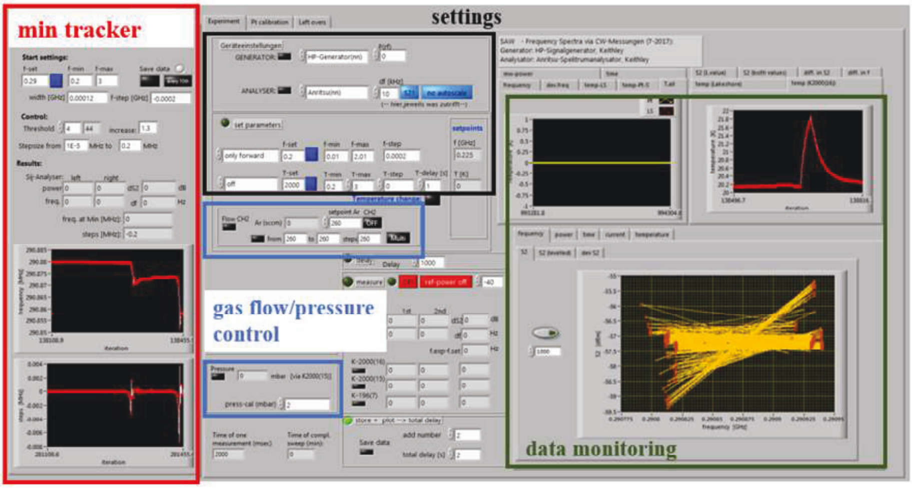

Figure 27: Labview control system for in-situ molecular layer detection. The minimum tracker and the MLD control have been added to the system.

Working principle

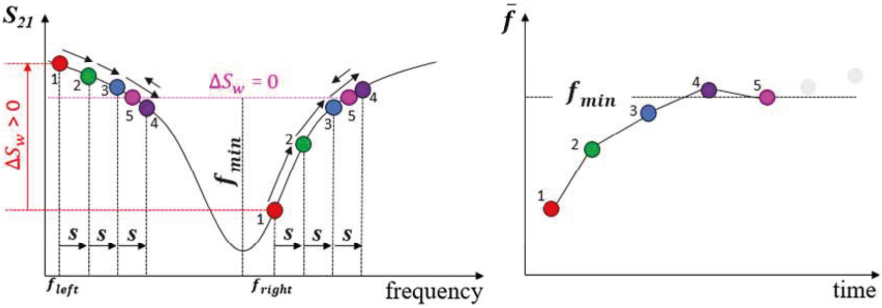

Figure 28: Schematic working principle of the minimum tracker.

The *minimum tracker* is a feedback control which measures the transmission S_{21} for two frequencies $f_{left} = \bar{f} - w/2$ and $f_{right} = \bar{f} + w/2$ with a fixed distance w nearby a minimum at f_{min} and tries to minimize the difference of their transmission:

$$S_{21}(f_{right}) - S_{21}(f_{left}) := \Delta S_w \rightarrow 0. \tag{11}$$

Assuming a symmetric minimum this would finally yield:

$$\bar{f} := \frac{f_{left} + f_{right}}{2} \rightarrow f_{min}. \tag{12}$$

Schematically the working principle of the minimum tracker is shown in Figure 28. Starting with $\Delta S_w > 0$ ($\bar{f} < f_{min}$) at the first cycle of the feedback loop, the frequencies f_{left} and f_{right} are enhanced by the step size s. Cycle by cycle the difference ΔS_w is becoming smaller. At the fourth cycle ΔS_wchanges sign, $\Delta S_w < 0$ ($\bar{f} > f_{min}$). Now s is inverted and reduced by 1/2. With every inversion of ΔS_w (and consequently $\bar{f}$), the step size s is reduced by 1/2. This way $\bar{f}$ and f_{min} are finally identical. In principle, the algorithm therefore allows to record the changes of two physical quantities:

(i) The change of the SAW velocity which causes a change of $f_{min} \approx \bar{f}$.

(ii) The change of the SAW attenuation which causes a change of the mean S_w :

$$\frac{S_{21}(f_{right}) + S_{21}(f_{left})}{2} := S_w \tag{13}$$

When an asymmetric minimum is formed, both variables are affected. Further effects, like a widening of the minimum (e.g. caused by a temperature gradient), an increase of the minimum (e.g. caused by a change of the background signal) and a decrease of the maximum (e.g. caused by SAW attenuation) only have an affect on S_w (Figure 29). The interpretation changes in S_w are therefore considerably more difficult.

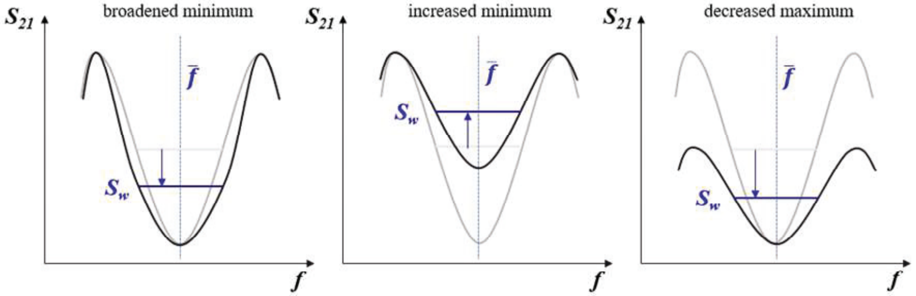

Figure 29: Schematic principle of the SAWs' intensity indication gained from the minimum follower.

In order to be able to follow a moving minimum, the step size can also be enlarged. This is typically done after the routine is moving $\bar{f}$ only in one direction for m (or more) times. The threshold m and the enhancement factor a have to be optimized in order to enable a perfect control of the sensor.

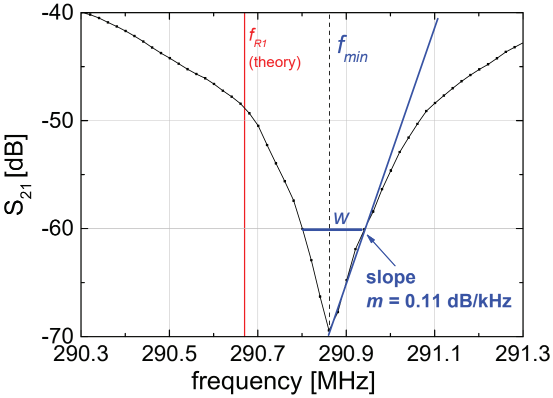

Figure 30: Minimum of S_{21} close to the theoretical resonance frequency of $LiNbO_3$ (YZ) using the developed SAW sensor. The sensors' resolution is given by the slope of S_{21} at the measured frequencies.

Since the *minimum tracker* is based on a minimization of ΔS_w its resolution depends on the resolution of S_{21} (typically ± 0.01 dB). Hence a frequency change $\Delta\bar{f}$ can be only recognized, if S_{21} changes at least by 0.01 dB. Therefore, the minimums' slope is decisive. For the recording a minimum close to the theoretical resonance frequency at the first harmonic of LNO has been chosen (Figure 30). Setting the width w to 120 kHz, the slope is 0.11 dB/kHz at -60 dB. This means that a change of 0.01 dB is induced by a frequency shift $\Delta\bar{f} = 90$ Hz which is finally the sensors' frequency resolution. Since a step size s smaller than 90 Hz is not practical, its lower limit has been set to 200 Hz (as compromise between frequency resolution and reacting time). In good approximation, $\bar{f}$ is denoted as f_{R1} in the following. Furthermore, the threshold and the enhancement factor were set to $m = 4$ and $a = 1.5$, respectively.

Since it turned out that the noise of S_{21} is increased at low transmissions (e.g. -60 dB) close to the resonance frequency, S_w has been smoothed over 11 points in all following measurements. f_{R1} is not strongly affected and is therefore smoothed only over 3 points.

4.4 INSTALLATION OF THE SAW SENSOR IN THE MLD CHAMBER

During the molecular deposition, physical parameters are changing inside the MLD chamber and SAWs are very sensitive to any perturbations at the surface. In order to correctly interpret the sensors response, it is therefore extremely important to understand and investigate the occurring effects. Vacuuming the chamber (4.4.1), temperature stability (4.4.2) and the influence of ozone and the microwave (4.4.3) are tested by making use of the *minimum tracker*.

4.4.1 Vacuuming

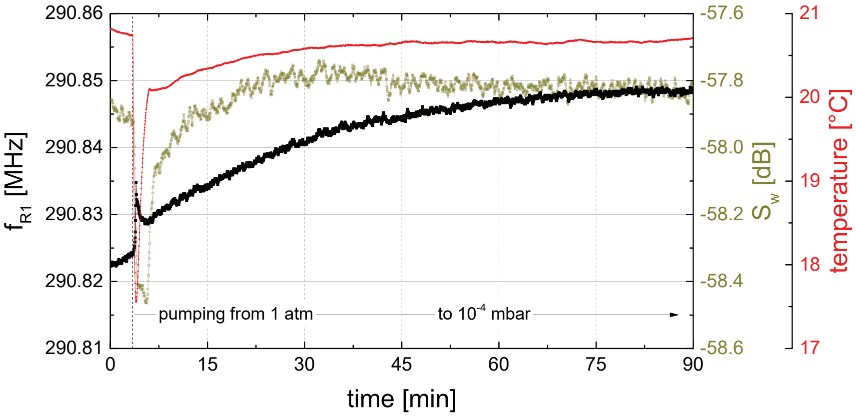

Figure 31: Development of resonance frequency, transmission and temperature in the first 90 minutes after mounting the developed SAW sensor inside the MLD chamber and pumping to a pressure of 10^{-4} mbar.

The device has been mounted inside the chamber at time 0 (Figure 31). At that time, the chamber is filled with atmospheric air. Starting the vacuuming, the temperature decreases abruptly, and consequently f_{R1} increases. After 45 min the temperature is stabilized. f_{R1} is stable after ~ 80 min with a noise of ± 500 Hz and an increase of ~ 25 KHz in total (since mounted inside the chamber). The SAW intensity first seems to decrease during vacuuming which is most likely an artefact of the *minimum tracker*. However, once f_{R1} is stabilized, the transmission S_w has stabilized as well.

The fact that it takes ~ 80 min before the system becomes stable might have various reasons:

(i) The temperature must be stabilized after vacuuming
(ii) Particles and molecules polluting the sensing area are removed
(iii) Moisture on the sensing area and on contacts is removed

Temperature effects are investigated in the following in more detail.

4.4.2 Temperature

It is known that LNO (YZ) has a large SAW velocity/frequency temperature coefficient of $94 \cdot 10^{-6}$ K^{-1}. Consequently, a change of temperature by 1 K is expected to change f_{R1} by 27 kHz. This is excellent for a temperature sensor, but a disadvantage for most other types of sensors based on SAWs. Therefore, it is very important to carefully study the temperature stability of our SAW sensor. Temperature changes at the devices inside the MLD chamber can have in principle three origins:

(i) Events inside the chamber like drastic pressure changes
(ii) Use of external (optical) heater
(iii) Change of the surrounding room temperature, for instance due to
  - thermal radiation of the surrounding
  - thermal conduction through cables and flange

In the following (ii) and (iii) are investigated.

Optical heater

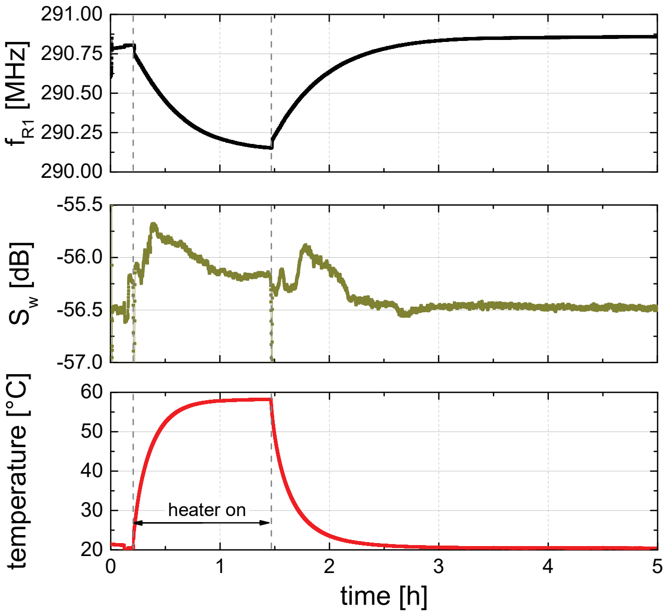

Figure 32: Temperature behaviour of the sensor for a heating process using the optical heater (4.1).

Using the optical heater, we can demonstrate the impact of the temperature on the sensor (Figure 32). Starting at time $t = 0$ min with the evacuation of the recipient, the optical heater is turned on to a power of 28.9 W after 10 minutes. The temperature of the sensor increases causing a decrease of f_{R1}. After ~ 1.5 h the temperature of the thermocouple has increased from room temperature to 58 °C whereas f_{R1} is decreased by ~ 700 kHz, which corresponds to a temperature change of 26 K (based on the literatures' SAW velocity temperature coefficient). Turning off the heater at 1.5 h causes an analogue increase of f_{R1} and stabilization after ~ 5 h. Generally the thermocouple reacts faster (increase/decrease and saturation) than the SAW sensor which might be caused by the difference in the optical absorption. This explains also the large difference in the final temperature for both sensors, thermocouple and SAW.

The transmission S_w seems to decrease during heating and during cooling as well. S_w is high, if the changes in f_{R1} are large, and it decreases if the changes in f_{R1} are decreasing. Qualitatively its tendency is comparable to the absolute derivative of f_{R1}, which might be caused by a temperature gradient on the sensor. The sharp minima while switching the heater on and off are artifacts of the *minimum follower*, since the step size s was too small (s = 5 Hz) during this first experiment, later on s was changed to s = 200 Hz.

Temperature stability

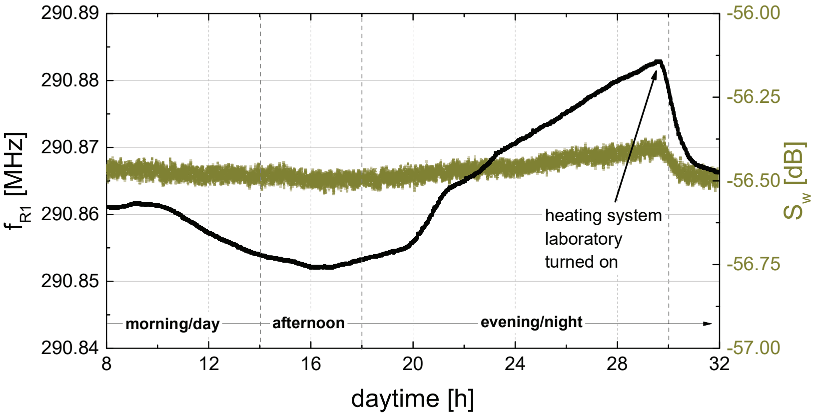

Figure 33: Temperature progression inside the MLD chamber and the SAW sensors' stability over an entire day.

Figure 33 shows a typical daily history of the SAW sensor recording. Its changes in transmission S_w and frequency f_{R1} are given in the Table 1 and might be mainly caused by changes of temperature. Based on the literatures' temperature coefficient, the corresponding temperature differences were determined and added.

The maximum change of 30 kHz corresponds to a temperature change of 1.1K. Most likely the change of the laboratory temperature is larger, so the thermal coupling between SAW sensor and room temperature might be reduced and/or delayed. However, with regard to the mass load sensitivity of LNO, frequency changes of a few kHz are expected for an MLD (see next chapter). Within the afternoon (2 pm – 6 pm) the system seems to be quite stable (shift of frequency < 1.5 kHz) which could make it possible to observe depositions. **Nevertheless, it would be best to stabilize the laboratory temperature for the developed sensor based on LNO**.

Table 1: Changes of the SAW sensors recordings (transmission S_w and frequency f_{R1}) and their theoretically corresponding changes of temperature for different times of a day.

	morning/day (6 am – 2 pm)	**afternoon** (2 pm – 6 pm)	**evening/night** (6 pm – 6 am)	**general**
f_{R1}	< 8.0 kHz (≙ 0.29 K)	< 1.5 kHz (≙ 0.05 K)	< 27 kHz (≙ 0.99 K)	< 30 kHz (≙ 1.1 K)
S_w	< 0.01 dB	< 0.01 dB	< 0.06 dB	< 0.06 dB

For the following investigation of the influence of the microwave generator and ozone to the SAW sensors' response, the long-term instability is not relevant.

4.4.3 Microwave and Ozone

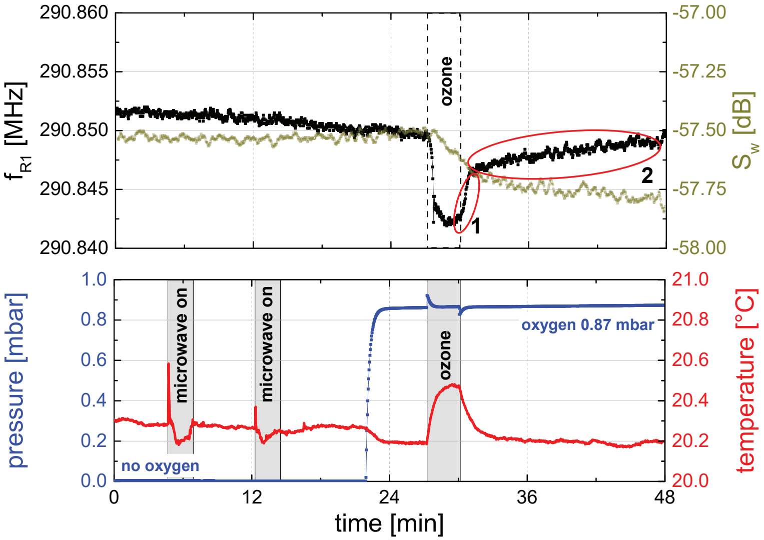

Figure 34: Stability of f_{R1}, S_w and thermocouple temperature caused by the microwave and ozone. The microwave is switched on during the grey intervals. Before switching on the third time, the chamber was filled with oxygen in order to create ozone.

Ozone is typically used for cleaning and activation of the substrates' surface, to obtain covalent bonds of the molecules on the substrate. After monitoring a molecule deposition, it might even be possible to remove the molecules by ozone treatment, and monitor this removal as well. The influence of the microwave and the ozone on a cleaned surface are therefore of interest. The microwave has been turned on twice without oxygen inside the chamber (vacuum), and once with oxygen (grey shaded intervals, Figure 34), which allows to create ozone. It is evident that:

Vacuum:

- The electromagnetic radiation of the microwave seems not to affect the SAW sensor, f_{R1} as well as S_w are stable.
- The thermocouple is affected by the microwave causing a reduced reading of the temperature of < 0.1 K as long as the microwave is turned on. This might be caused by an electronic coupling of microwave and thermocouple.

Oxygen and ozone:

- Turning on the microwave, ozone rapidly seems to heat the thermocouple by ~ 0.3 °C in 3 min.
- Ozone affects the SAW sensor and reduces f_{R1} and S_w by ~ 7 kHz and ~ 0.3 dB, respectively.
- Stopping the ozone treatment, the thermocouples' temperature drops to its original state within a few minutes.

- The reduction of f_{R1} partially recovers in less than one minute (by 4 kHz, see ellipse 1), but a remaining increase of ~ 3 kHz is present, which takes ~ 20 min (see ellipse 2). This indicates that two effects might affect the SAW under ozone treatment. On the one hand, this can be a temperature effect. On the other hand, the ozone can cause surface charges which disturb the electric fields in the piezoelectric substrate.
- In contrast to the shift of f_{R1}, the shift of S_w is persistent even after more than 15 minutes.

In summary, the microwave itself seems not to affect the SAW sensor. However, the ozone has an impact on f_{R1} and S_w. These impacts are given by the ozone connected temperature changes at the sensor and possible removal of material from the sensor.

Chapter 5: Experimental results and discussion

Various KNNO thin films, prepared by PLD or MOCVD, have been tested as candidates for the SAW sensor (full list, Appendix A). This test is based on a ferroelectric characterization by using IDEs (plane capacitor electrodes) and on measurement of the SAW signal. Sample *47_008_SSO* fabricated by MOCVD showed the best SAW properties and has been used as a SAW sensor. Furthermore bulk LNO (YZ) has been used as a reference and is compared to literature (5.1).

Based on the determined material properties in (5.1), the developed SAW sensor for a molecular deposition has been tested on MLD of APTES. An attempt has been made to in situ monitor the deposition and removal of APTES in our MLD chamber (5.2).

5.1 MASS SENSITIVITY OF LITHIUM NIOBATE AND KNNO ON SSO

Here, the mass sensitivity of thin film $K_{0.7}Na_{0.3}NbO_3$ on $SmScO_3$ (110-cut) in Z propagation direction (in the following abbreviated by KNNO) is investigated. Additionally, this is compared to $LiNbO_3$ (Y-cut) in Z propagation direction (LNO). Due to historical reasons, it should be noted that the measurements on LNO were carried out using the SMA-X(gold), a Twist180g3 design and the PVC cover (so the CuBe springs for mounting are not used). The electrode structure of the KNNO sample, however, is different and cannot be used in this sample holder. These measurements were performed on the standard sample holder (3.3.1). More detailed information about both samples (with names 47_008_SSO and LNO_503_Tw180g3_5) are given in the appendix (page 60).

Basically both materials are covered with PMMA using a spin coater. The PMMA layer thickness is determined by a stylus profilometer, and consequently the SAW velocities are determined using the beating frequency.

On this basis we show

(i) a direct comparison of the SAW properties of both materials without mass load (5.1.1).

(ii) that the analysis of SAW intensity is rather difficult with both setups, but an indication that the thin film material might be more suitable for detecting small layers (5.1.2).

(iii) a comparison of the materials’ mass sensitivities and finally the answer whether the KNNO thin films are preferable as sensors (5.1.3 and 5.1.4).

5.1.1 LNO and KNNO without mass load

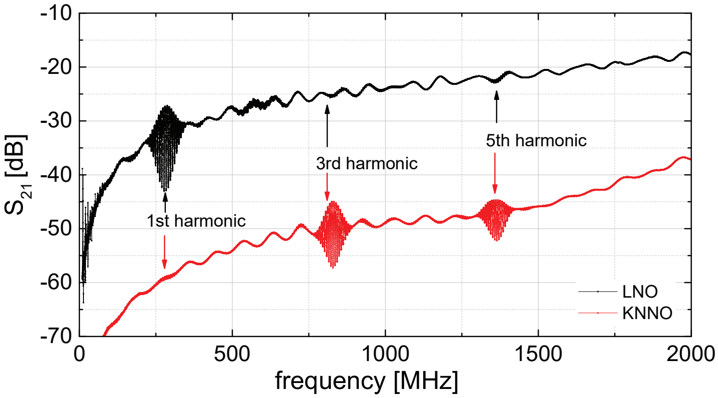

Figure 35: Frequency spectrum of S_{21} for $LiNbO_3$ (YZ) (LNO_503_Tw180) and $K_{0.7}Na_{0.3}NbO_3$ on $SmScO_3$ (110-001) (47_008_SSO). The 1st, 3rd and 5th harmonics are marked.

Figure 35 shows the frequency spectrum of S_{21} including the 1st, 3rd and 5th harmonics for both samples. The fact that a bulk material is compared with a thin film, and the use of different sample holder leads to strongly different electric background and a different spectrum.

For a better comparison of single harmonics, the spectra are shifted in Figure 36. The bulk material shows the largest signal at the fundamental mode, whereas the thin film KNNO has its highest intensity at the 3rd harmonic (Figure 36 (d)). Although the intensities of the 3rd and 5th harmonic of LNO and the 1st harmonic of KNNO are very weak, the velocities can be determined very well by investigating the beating frequency (equation (*6*), (*8*)). They are determined to (3470 ± 10) m/s and (3370 ± 10) m/s for LNO and KNNO, respectively. They differ only by 3% and are individually in perfect agreement with literature [9], [7].

This means, both systems (samples and sample holder) show reasonable results and can be used to investigate the mass load sensitivity.

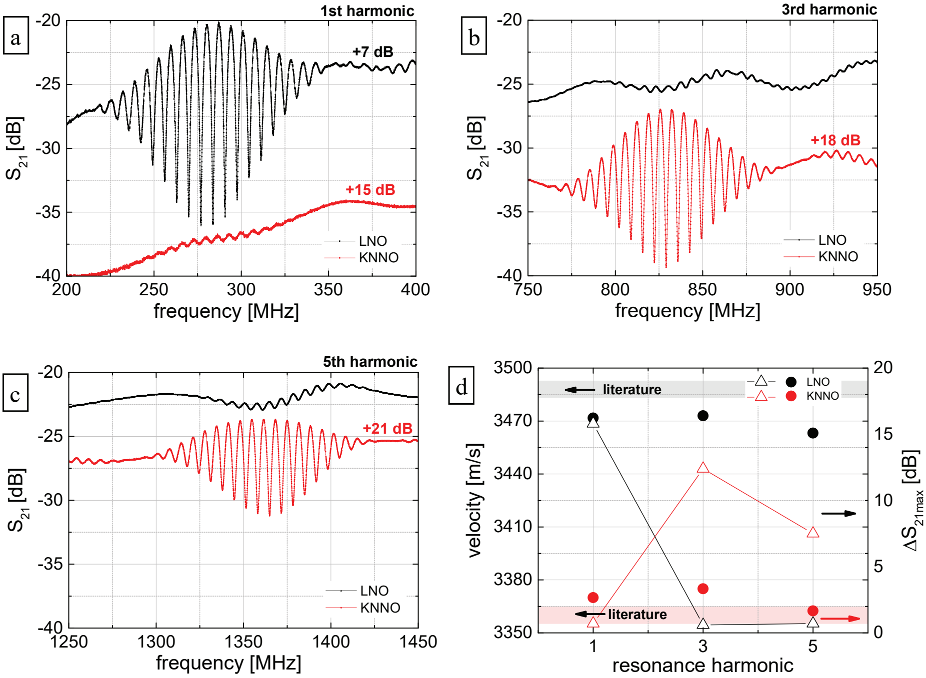

Figure 36: Transmission coefficient of 1st (a), 3rd (b) and 5th (c) harmonic of LiNbO$_3$ (YZ) (LNO_503_Tw180) and K$_{0.7}$Na$_{0.3}$NbO$_3$ on SmScO$_3$ (110-001) (47_008_SSO). The velocities of the SAW determined by equation (6) *and the SAW intensities (d) together with the literature values for the velocity (shaded areas) for the different materials KNNO (red) and LNO (gray) for the different harmonics.*

5.1.2 Attenuation due to mass load

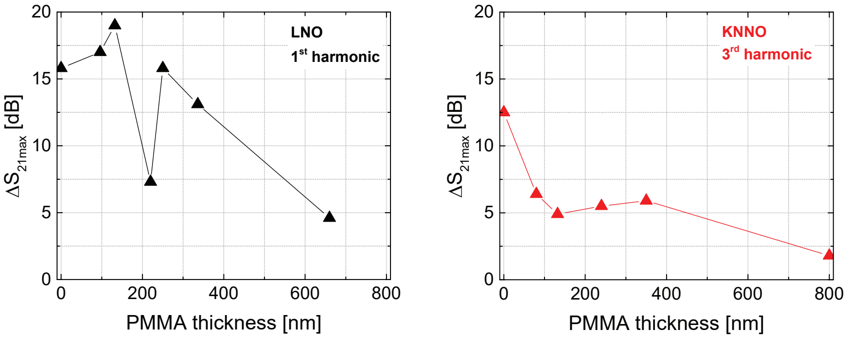

Figure 37: SAW intensity of $LiNbO_3$ *(YZ) (LNO_503_Tw180) and* $K_{0.7}Na_{0.3}NbO_3$ *on* $SmScO_3$ *(110-001) (47_008_SSO) as a function of PMMA mass load.*

According to the simple theoretical picture given in (2.4) there is supposed to be no effect of the mass load on the attenuation. However, this approach assumes that no energy dissipation occurs. Therefore the impact of the mass load on the transmission coefficient is investigated first. Since the SAW intensity is highest for the 1st harmonic and the 3rd harmonic of LNO and KNNO, respectively, these are exemplary examined. PMMA layers of different thicknesses are deposited on top of the samples and ΔS_{21} and finally ΔS_{21max} have been determined (3.3.2). The results are shown in (Figure 37). It is evident that:

(i) Both samples show an effect on the intensity and
(ii) no reliable dependence is visible.

Therefore we conclude that the installation and hence measurements are not reproducible (because of PVC cover (4.1.4), bonding (3.3.1)). To analyze the attenuation, the setups need be optimized. Nevertheless, the beating frequency and thus the SAW velocity as a function of PMMA mass load can be determined reliably (see next section, 5.1.3).

5.1.3 Velocity changes due to mass load:

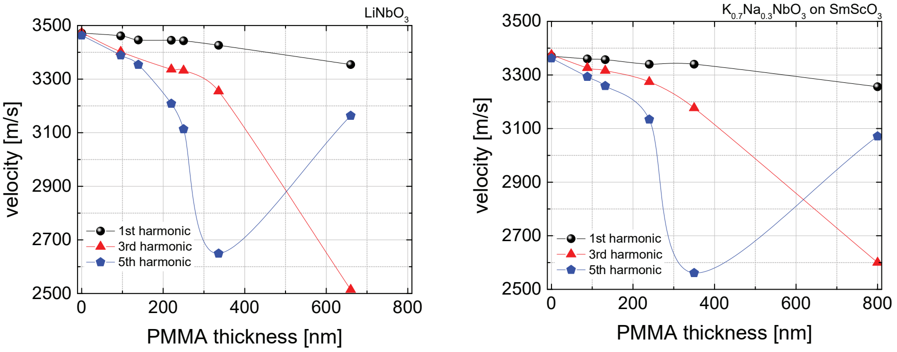

Figure 38: SAW velocity dependence on the PMMA layer thickness for 1^{st}, 3^{rd} *and* 5^{th} *harmonic for* $LiNbO_3$ *(YZ) (LNO_503_Tw180) and* $K_{0.7}Na_{0.3}NbO_3$ *on* $SmScO_3$ *(110-001) (47_008_SSO).*

Alternatively, the beating frequencies can be investigated for different layer thicknesses of PMMA and the SAW velocities have been determined (equation (*6*)) for LNO and KNNO. The resulting velocities depend on the one hand on the operating frequency f_{Rn}, hence on the IDT design and harmonic, and on the other hand on the mass density of PMMA. It is evident that:

(i) Without a mass load, the velocity does not depend on the frequency (within the accuracy of determining the beating frequency).

(ii) The velocity decreases, due to a mass load (there are exceptions for the fifth harmonic at 660 nm for LNO and 800 nm for KNNO).

(iii) The decrease in velocity is frequency dependent. The higher the frequency, the stronger the decrease (in agreement with equation (*8*)).

(iv) The linearity between mass load and velocity is limited. Moreover the linear regime seems to be frequency dependent. For the first harmonic the velocity is linear up to ~ 350 nm of PMMA. For the 3^{rd} and 5^{th} harmonic, this linear regime is much smaller.

Apart from the fact that the free particle surface velocity of KNNO is about 100 m/s lower compared to LNO, their dependence on a mass load seems to be qualitatively and quantitatively comparable. But the theoretical approach (2.4) and its predicted linear decrease of velocity are only partially valid. This is analysed more in detail in the next section.

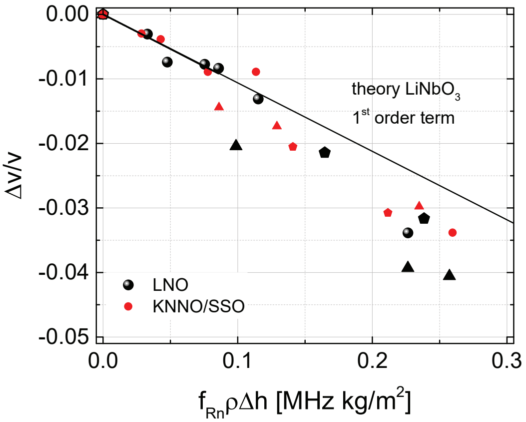

Figure 39: Relative velocity change independent of the deposited materials' mass density and independent of the operating frequency (IDT design) for LiNbO$_3$ (YZ) (LNO_503_Tw180) and K$_{0.7}$Na$_{0.3}$NbO$_3$ on SmScO$_3$ (110-001) (47_008_SSO) as a function of normalized mass load.

To compare both materials with each other and with literature, it is more reasonable to look at the relative velocity change $\Delta v/v$ independent of the IDTs' design and mass density of the deposited material. Figure 39 shows $\Delta v/v$ versus $f_{Rn}\rho\Delta h$ of the data shown in Figure 38. The resonance frequencies f_{Rn} are determined from the measurement without any mass load, the mass density ρ of PMMA is 1180 kg/m^3 and Δh represents the thickness of the PMMA layer. The resulting materials' sensitivity c_m is directly given by the slope

$$c_m = -\frac{\Delta v/v}{f_{Rn}\rho\Delta h}. \tag{14}$$

Within a small regime of $f_{Rn}\rho\Delta h$ < 0.08 MHz kg/m^2, a linear approach describes the velocity changes sufficiently well (Figure 39) and moreover perfectly agrees with the literature value of LNO (by neglecting the elastic properties of PMMA) [7]. The materials' sensitivities can be determined by linear fitting (in the regime $f_{Rn}\rho\Delta h$ < 0.08 MHz kg/m^2 and with fixed y-axis intersection at $\Delta v/v = 0$) and summarized in Table 2.

Table 2: Sensitivity to mass load for LiNbO$_3$ (YZ) (LNO_503_Tw180) and K$_{0.7}$Na$_{0.3}$NbO$_3$ on SmScO$_3$ (110-001) (47_008_SSO) at small respectively large mass load and/or frequency.

	LNO (literature)	**LNO (measurement)**	**KNNO**
C$_m$ [m^2/(MHz kg)] ($f_{Rn}\rho\Delta h$ < 0.08 MHz kg/m^2)	0.107	0.11 ± 0.01	0.11 ± 0.01
C$_m$ [m^2/(MHz kg)] ($f_{Rn}\rho\Delta h$ = 0.5 MHz kg/m^2)		~ 0.9	~ 0.9

There is a perfect agreement between literature and the measured values. It is even not possible to distinguish the literature curve and the fitted ones, since they are almost congruent. Finally, KNNOs' thin film sensitivity c_m seems to be identical to the sensitivity of bulk LNO. And since there is perfect agreement with the theory, neglecting the elastic properties of PMMA, the sensitivity of c_m= 0.11 $m^2/(MHz\ kg)$ can be used for various deposition materials with similar viscoelasticity.

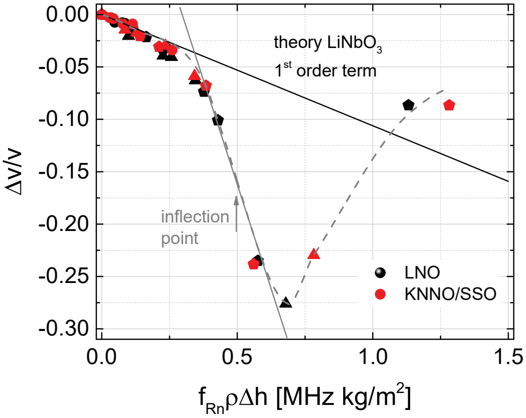

Figure 40: Relative velocity change independent of the deposited materials' mass density and the operating frequency (IDT design) for $LiNbO_3$ (YZ) (LNO_503_Tw180) and $K_{0.7}Na_{0.3}NbO_3$ on $SmScO_3$ (110-001) (47_008_SSO) up to high mass load and frequencies.

However, a strong deviation from the linearity is visible (grey dashed line in Figure 40) if we move to larger mass load and frequency. Qualitatively this is in perfect agreement with the numerical solutions of the theoretical approach demonstrated in [7]. According to this theory, the origin of the non-linearity is based on an upcoming difference of phase and group velocity of the SAWs. This means the deposited layer causes dispersion of the Rayleigh wave. Consequently, the assumption of the simple linear approach of a layer moving synchronously with the piezoelectric material becomes wrong at high mass load and/or frequencies.

The non-linearity of $\Delta v/v$ also offers a great opportunity. The grey dashed line is a guide for the eye. At its inflection point (at 0.5 MHz kg/m^2) the slope reaches its maximum and is 0.9 (MHz kg/m^2)$^{-1}$. Compared to the small linear regime, the sensitivity is increased by a factor of almost 9, which shows the potential for sensor applications. This significantly increased sensitivity of the sensor could be achieved by

(i) depositing an additional layer (e.g. SiO_2, with f_R = 300 MHz a layer thickness of ~ 630 nm or ~ 130 nm would be necessary for LNO or KNNO, respectively) which could also offer the possibility to use the sensor in liquids by transforming the Rayleigh-type sensor into a Love-type sensor.

(ii) choosing a higher frequency

(iii) combining (i) and (ii).

The necessary parameters to achieve this enhanced sensitivity can be easily determined from Figure 40.

5.1.4 Summary

The comparison of the mass load sensitivity of bulk LNO and thin film KNNO showed:

(i) The determined velocities from the beating frequency show reliable results. However, an analysis of the SAW attenuation due to mass load is almost impossible with the used setups. An optimized setup has been used for the MLD in the next chapter.

(ii) Compared to bulk LNO the thin film KNNO showed a much higher SAW intensity at higher frequencies. This indicates a higher energy confinement at higher operating frequencies in the thin film.

(iii) Based on the relative velocity change thin film KNNOs' sensitivity (to mass load) c_m seems to be identical to the sensitivity of LNO (both investigated in Z propagation direction). Thus, at the same operating frequency the seemingly higher energy confinement (see (ii)) did not lead to a higher sensitivity c_m. However, according to the frequency dependent intensity distribution, thin film KNNO seems to be more applicable at higher operating frequencies. Since the relative velocity change scales with frequency (equation (8)), a sensor based on thin film KNNO has potentially a much higher sensitivity. But it should be made clear that the potentially higher sensitivity might be ultimately based on the use of a thin film and not on the materials' elastic properties.

(iv) For both materials, the simple linear theoretical approach (2.4) underestimates the sensitivity c_m at higher frequencies and mass loads due to an upcoming dispersion of SAWs. But this could be used to significantly increase the sensors' sensitivity even more (by a factor of ~ 9).

Finally, thin film KNNO seems to be potentially very well applicable as a mass detector at high frequencies. Therefore it is most likely more sensitive. Nevertheless, due to the lack of suitable KNNO films an attempt has been made to monitor an in situ MLD of APTES via LNO SAW sensors (next sections).

5.2 IN-SITU MONITORING MLD

One of the major aims of this work was to develop and test SAW sensors which are able to in situ monitor the MLD. The setup has been tested with a LNO SAW sensor which was installed in the chamber (4.4). It showed very promising frequency resolution and sensitivity. Nevertheless, monitoring the MLD itself is the real challenge.

In this chapter we show

(i) the calibration of a SAW sensor for APTES depositions based on the results of the previous sensitivity analysis (5.2.1) and

(ii) an example of an in situ monitoring of APTES deposition and an subsequent APTES removal with ozone (5.2.2).

5.2.1 Sensor Calibration

With deposition of PMMA the mass load sensitivity of LNO has been determined by the beating frequency f_b to $c_m = (0.11 \pm 0.01)$ m^2/MHz kg for the linear regime. Using the *minimum tracker* for monitoring the MLD, the resonant frequency f_{R1} (or a minimum of the interference pattern close to f_{R1}) is tracked (4.3). Furthermore, the MLD is done with APTES (ρ = 1180 kg/m^3). With a theoretical fundamental resonance frequency of 290.67 MHz (3.3.1) and using equation (*8*) we obtain a sensitivity (assuming a molecular density equivalent to the liquid state) of:

$$\Delta h = -\frac{\Delta f_{R1}}{f_{R1}^2 c_m \rho} = -\frac{\Delta f_{R1}}{(11 \pm 1)} \text{nm/kHz} . \tag{15}$$

The shift Δf_{R1} depend on the mass load per unit area and thus also on the density of the load. With a frequency resolution of 200 Hz (step size of the algorithm, (4.3)) the resulting resolutions of the effective thickness Δh, the mass density per unit area $\rho\Delta h$ and the mass Δm are summarized in Table 3. For the mass resolution, a sensing area (500 x 500) µm^2 is assumed.

Table 3: SAW sensor resolutions based on the fundamental resonance frequency of 290.67 MHz and a frequency resolution of the sensor of 200 Hz (actually a frequency resolution of 90 Hz is possible but the minimums trackers' *step size s is set to s = 200 Hz, see section 4.3).*

	Δf_{R1}	Δh	$\rho\Delta h$	Δm
resolution	200 Hz	0.02 nm	2.15 ng/cm^2	5.4 pg

5.2.2 In situ monitoring

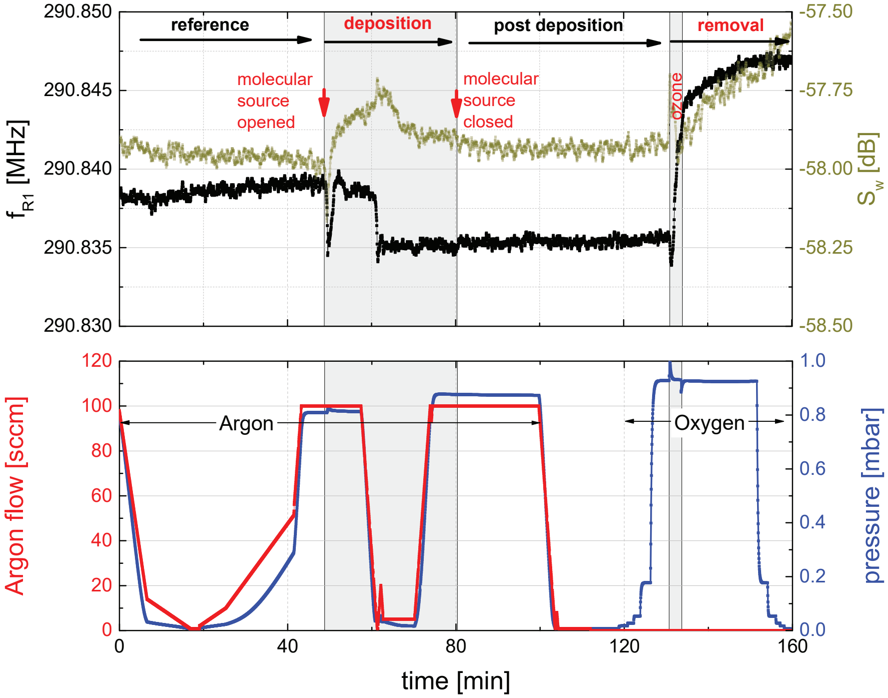

Figure 41: Chronological overview of the in situ monitoring of a MLD process for APTES including the SAW sensors' response of frequency and intensity. The process is controlled by Argon flow.

For the proof of principle, a deposition and removal of APTES has been monitored. In contrast to the usual deposition process, no activation was performed before. Hence the sensor might be initially covered by moisture or organic contaminations. A chronological overview of this experiment, including the sensors' response, is shown in Figure 41. The experiment can be subdivided into four parts, which are investigated more in detail.

(i) **Reference:** Stability check of the sensors response during decreasing and increasing argon flow including the resulting pressure change. This part is used as a reference for the following deposition. Despite the pressure change the SAW signals f_{R1} and S_w only show a very small drift in the regime. The frequency of the minimum changes by less than 1 kHz during 50 minutes, which might be caused by small temperature drifts.

(ii) **Deposition:** Ranging from opening to closing the molecular source. During this time the argon flow is reduced which initializes the actual APTES deposition (discussion below)

(iii) **Post deposition:** During this time the recipient is fluted with oxygen, APTES might bind or adsorb (discussion below).

(iv) **Removal:** Ozone plasma is created by the microwave generator and cracks the organic molecule APTES (discussion below).

The process parts (ii) – (iv) are discussed in detail in the following.

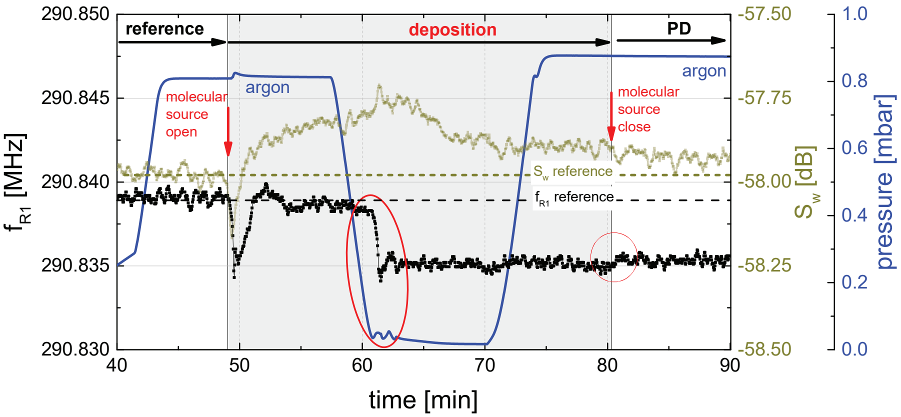

Figure 42 and Table 4: Gas phase deposition process of APTES monitored by the SAW sensor. Opening and closing of the molecular source, as well as a pressure controlled deposition can be monitored. The features in frequency f_{R1} and transmission S_w and their interpretations are listed in the table.

time [min]	**pressure p**	$\boldsymbol{f_{R1}}$	$\boldsymbol{S_w}$	**interpretation**
40 - 48	increased from 0.25 mbar to 0.81 mbar	~ constant at 290.8391 MHz (reference)	~ constant at -57.98 dB (reference)	With a closed molecular source the sensors' response is stable, even for a change of pressure.
49 - 52 **open source**	small peak when opening the source	sudden decrease by 3.8 kHz followed by an increase back to reference	sudden decrease to -58.17 kHz followed by a steady increase	Peak in pressure indicates evaporation of the source due to overpressure in the source. Change of f_{R1} indicates a mass load which almost immediately vanishes. Sudden decrease of S_w might be an artefact of the minimum follower. The following total increase might be an increase of the background signal.
52 - 58	0.81 mbar	slow decrease of f_{R1} by ~ 800 Hz	further increase by ~ 0.05 dB	f_{R1} indicates a mass load caused by a slow deposition of APTES. This deposition might lead to a further increase of the background signal
58 - 63	decreased to 0.034 mbar followed by an increase to 0.05 mbar	sudden decrease by 3.8 kHz to a stable value starting at 0.034 mbar	further increase by ~ 0.06 dB	Reaching 0.34 mbar APTES seems to be deposited. After a short time the mass load seems to be constant (more details in Figure 43). The increase of S_w might be another artefact of the *minimum tracker*, due to the change of f_{R1}.
63 - 81	further slow decrease to 0.017 mbar followed by an increase to 0.87 mbar	no significant effect	decrease by 0.03 dB, but still above reference value	The sensor seems to be still coated with APTES, f_{R1} indicates no change in mass load. The decrease of S_w might be significant since the frequency is stable at this time, but an interpretation is hardly possible.
81 - 100 **close source**	0.87 mbar	no significant change	no significant change	A layer of APTES is deposited and recorded by the sensor.

The main features of the APTES deposition are shown and described in Figure 42 and Table 4. The following points are observed:

(i) Although S_w shows some characteristics, their interpretation is difficult. In most cases artefacts of the recording (*minimum tracker*) cannot be excluded. An improved version of the *minimum tracker* might help. Especially the features during pressure induced deposition are extremely interesting and could be investigated with an improved *minimum tracker* in more detail.

(ii) The recording of f_{R1} shows features that can be easily interpreted:

a) Opening the molecular source: The frequency f_{R1} is temporary decreased, which is accompanied with a small peak in the pressure. A temporary mass load is recorded. The molecular density might be too low to cause a stable deposition and the physisorbed molecules seem to be desorbed again as indicated by the immediate return of f_{R1} to its reference value. But the observed process might give information about the residual time of the molecules on the surface.

b) Pressure controlled APTES deposition (separately shown in Figure 43):

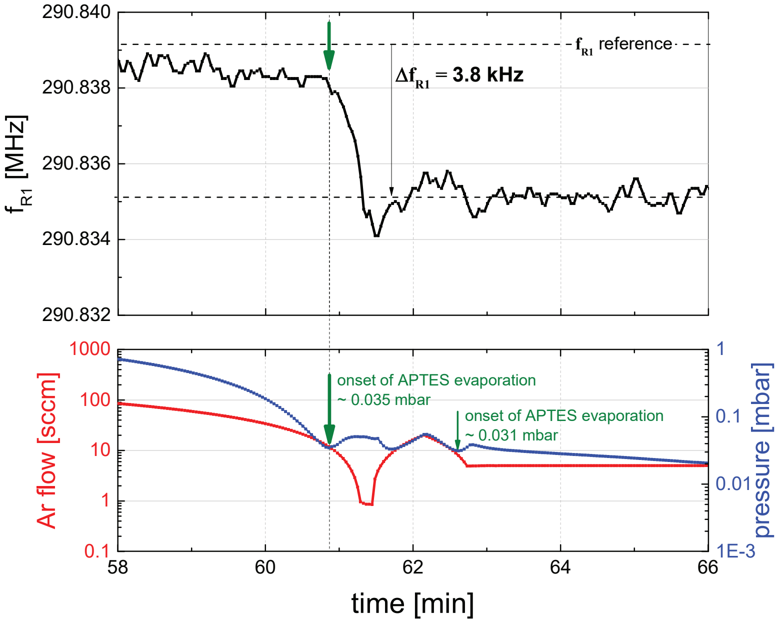

Figure 43: Resonance frequency and pressure progression while decreasing the argon flow with an open molecular source. The frequency f_{R1} drops by 3.8 kHz at the evaporation onset of APTES (green arrow).

Starting at a pressure ~ 0.81 mbar the argon flow is successively decreased in order to start the APTES deposition in a controlled way. At a pressure of 0.035 mbar f_{R1} is suddenly decreased. This is accompanied by an increase of the pressure, although the argon flow is still decreasing. Below 0.035 mbar APTES seems to evaporate (vapor pressure of APTES 0.02 mbar at 20°C, [10]) and causes a very fast deposition process on the sensor. The sudden onset of evaporation slightly increases the pressure in the chamber and at the same time f_{R1} is decreased due to the deposited mass. A renewed increase and subsequent decrease of the argon flow shows that the event in pressure and thus evaporation of APTES can be repeated, but this time f_{R1} is no further decreasing but stable. It might be that the surface is already saturated with molecules due to the previous fast deposition (usually an argon pressure of 0.1 mbar is used for APTES deposition) and an equilibrium state with the surrounding has been reached. Also interesting is the fact, that the temporary deposition of molecules by opening the source seems to be of the same amount (decrease of f_{R1} is comparable). According to the sensor calibration (equation (15)) the total decrease of $\Delta f_{R1} = 3.8$ kHz is equivalent to an effective layer thickness of 0.35 nm of APTES.

c) Closing the molecular source: Upon closing the source, a small initial enhancement of f_{R1} by ~ 400 HZ is visible. After that f_{R1} seems to be stable and hence the mass load is expected to be stable. This also applies during post-deposition, when argon is pumped out and oxygen is introduced into the chamber. Closing the source, the surrounding concentration of molecules vanishes, which might change the equilibrium state to a lower molecule density at the sensors surface. The mass load is finally slightly reduced.

In summary, the developed SAW sensor impressively demonstrated the molecular deposition of APTES. In addition, several characteristics have been observed like the temporary decrease of f_{R1} by opening the source or the small enhancement of f_{R1} by 400 Hz by closing the source. Confirming these characteristics in further performed depositions might give insight to the molecular deposition process itself and its perfect process conditions. With respect to the measurement of the transmission S_w, although there are features visible, there is still space for improvement. In the following the removal process via oxygen plasma is tried to be monitored as well.

Removal of APTES

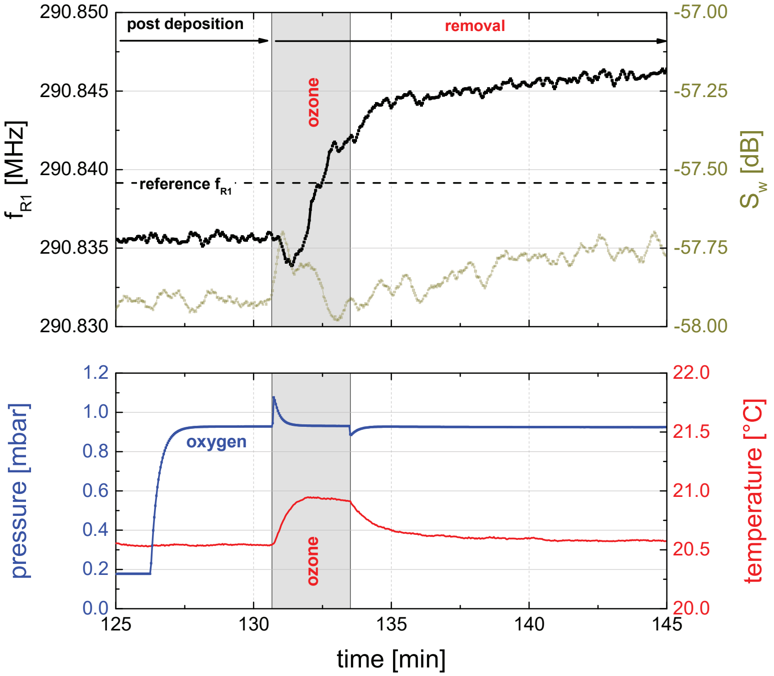

Figure 44: SAW sensors' frequency response f_{R1} and thermocouple temperature progression due to an ozone plasma treatment after a deposition of APTES.

Oxygen plasma can also be used to remove the deposited APTES molecules. Before APTES deposition, the sensors response to ozone has already been investigated (4.4.3). It turned out that the ozone heats up the sensors surface which leads to decrease of f_{R1}. The reduction of f_{R1} stays during the plasma treatment and releases afterwards within at least 15 minutes. An ozone treatment after the previously investigated APTES deposition is shown in Figure 44. During the post deposition and while flooding the chamber with oxygen (~ 0.9 mbar) no significant change of f_{R1} and S_w occurs. The surface still seems to be covered with APTES before starting the ozone treatment. Igniting the ozone plasma by turning on the microwave generator, the following points are observed:

(i) S_w shows a similar characteristic behavior as it was observed during the temperature increase caused by the optical heater (4.4.2). This tendency might be connected to the sudden change of f_{R1} and needs more experiments to be completely understood.

(ii) Again the frequency response f_{R1} is much easier to be interpreted:

   a. Starting the ozone plasma: The resulting increase in temperature (thermocouple) is accompanied by a first decrease in f_{R1}. After about one minute an increase of f_{R1} sets in whereas the temperature continues to rise. Most likely the first decrease of f_{R1} is caused by an increasing temperature of the sensors surface. Since the ozone plasma cracks APTES molecules at the same time, a removal of molecules is starting. At the minimum of f_{R1} this (f_{R1} increasing) effect of removal exceeds the (f_{R1} decreasing) temperature effect.

b. Stopping the ozone plasma: Although the temperature immediately decreases, f_{R1} still increases. This seems to be caused by the cooling of the sensor visible also in the thermocouples' temperature signal (compare 4.4.3). However, the frequency is now at least 7 kHz higher than the reference value (dashed line). Before the deposition of APTES the sensor had not been cleaned. Hence, the initial contamination of moisture or particles might be removed as well, which would lead to an enhanced value of f_{R1}.

Also the removal of APTES seems to be clearly detected by f_{R1}. Since the sensor has not been activated/cleaned before the deposition the interpretation of its signal is more complex, but still consistent with previous investigations (4.4.3).

5.2.3 Summary

The in situ monitoring of an APTES deposition and removal process in our MLD chamber with the new SAW sensor showed the following results:

(i) Based on frequency changes, the sensors' resolution has been determined to 0.02 nm, which is significantly below the thickness of the envisioned APTES layer (based on the mass density of APTES), and thus should allow an in situ monitoring of the MLD process.

(ii) The interpretation of the SAW intensity S_w recorded via the *algorithm minimum tracker* turned out to be difficult. Here a more complex algorithm might have to be developed.

(iii) In contrast, the frequency measurement f_{R1} perfectly monitors the deposition and removal of APTES. The developed sensor is able to detect the molecular deposition and can be interpreted. The effective thickness of deposited APTES on LNO is determined to 0.35 nm according to the calibration.

(iv) By opening the molecular source a temporary deposition has been observed, which might reveal information about the residual time of molecules on the surface.

(v) By closing the source, a seemingly decrease of the mass load has been observed, which might be caused by a changed equilibrium state of adsorption and desorption of molecules on the surface.

Thus, the sensor might give new insight to the molecular deposition process itself. The understanding and interpretation of the sensor will develop if more and different MLD processes are recorded and the algorithm is optimized.

Chapter 6: Conclusion and outlook

The main goal of the work was to develop a molecular mass detector based on surface acoustic waves, which can among others in situ monitor the adsorption and desorption of molecules. Monitoring the gas-phase MLD, this should provide information about the deposition process itself and ultimately improve the controlled production of self-assembled organic monolayers. The basic idea was to use epitaxial thin films of KNNO as piezoelectric substrate, which due to their properties (large piezoelectricity, lead-free, tunable SAWs) are very promising for bio applications. This should be compared to conventional bulk material of LNO. Finally a recording of a typical molecular deposition process has been performed with the developed mass detector.

SAW Sensor development

An extremely sensitive mass detector in this first step (based on LNO bulk) with a **resolution of 0.01 nm** (for the layer thickness of APTES in liquid state) has been manufactured. The following progresses have been achieved:

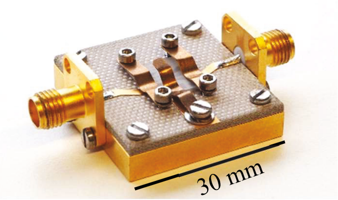

Figure 45: The new SAW sensor

- A sample holder was developed, which not only allows a very fast, reproducible, reliable and simple contacting but also the application in our home-made MLD chamber even under the use of ozone plasma.
- Using electron-beam lithography a sample design has been developed which includes a temperature sensor and interdigital transducers for ferroelectric film characterization and SAW measurements in different directions. Theoretically the total electric losses are below 6.5 dB.
- The typically used lift-off process has been improved by adding an additional plasma ashing step and determining an optimum electron-beam dose leading to seemingly better mechanical adhesion and electric coupling of the electrodes.

Comparison of thin film KNNO and bulk LNO

Several KNNO thin films have been tested as candidates for the SAW mass detector. Unfortunately only one sample has been found which meets the requirements (especially a high SAW intensity around room temperature). Nevertheless a comparison of the mass load sensitivity with LNO bulk could be achieved and has shown that:
In general, the sensitivity to mass load for both thin film KNNO and bulk LNO seems to be identical.

- In the linear regime of small mass load and operating frequency a perfect agreement with the literature (c_m= 0.11 m^2/(MHz kg) for LNO) has been found.

- For higher frequencies and mass loads the sensitivity seems to increase and reaches a maximum at $f_{Rn}\rho\Delta h$ = 0.5 MHz kg/m^2 with a total increase of a factor 9. Qualitatively this is in agreement with numerical solutions.
- However, according to the frequency dependent intensity distribution, thin film KNNO seems to be more applicable at higher operating frequencies and may enable therefore a much higher SAW sensor resolution.

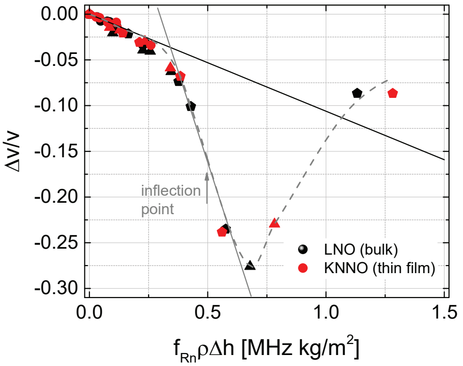

Figure 46: Relative velocity change for LiNbO3 (YZ) and K0.7Na0.3NbO3 on SmScO3 (110-001) up to high mass load and frequencies.

In situ monitoring of MLD

As a proof of principle of the new SAW mass detector an in situ deposition of APTES molecules has been recorded. Due to a lack of applicable KNNO thin films this had to be performed with most likely less sensitive LNO bulk. This first test was successful and revealed:

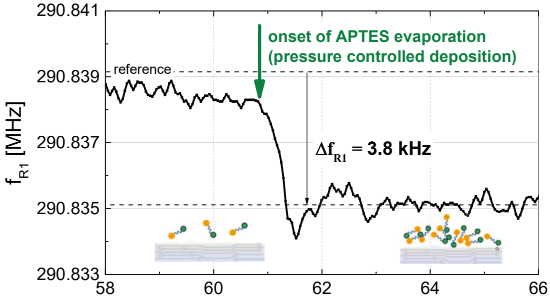

Figure 47: Frequency response of the SAW mass detector during a pressure controlled deposition of APTES molecules.

- The frequency measurement perfectly monitors the deposition and removal via ozone of APTES.
- After the evaporation of APTES a stable mass load has been observed which corresponds to 0.35 nm assuming the density of liquid APTES.
- During and after closing the molecular source a temporary deposition and a seemingly decrease of the mass load has been observed, respectively. These features might reveal information about desorption and adsorption processes of the molecules on the surface.

In summary, it has been demonstrated that the developed SAW detector can in situ monitor molecular deposition and removal in our MLD chamber. The detector finally offers the possibility to bring light into the “dark of the black box of molecular layer deposition” and, to go one step further, in finding optimum deposition conditions and, finally, in the fabrication of perfect interfaces between organic and inorganic materials. So this work might set the starting point for these investigations. But apart from the detection of molecules, the new SAW detector might be a basis for other interesting sensor applications in or outside the field of biosensor technology.

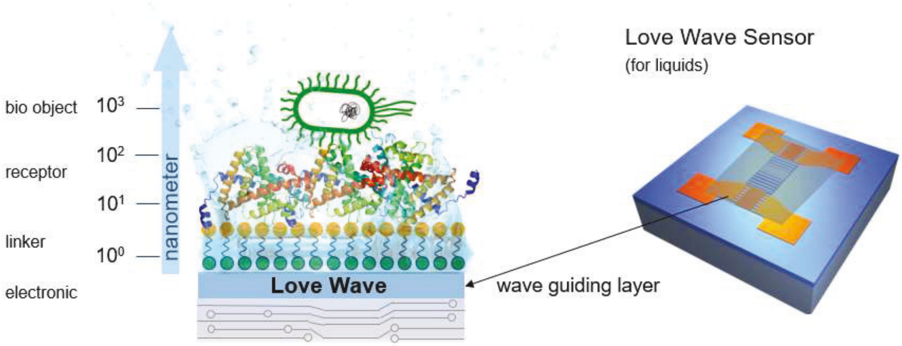

Figure 48: Schematic principle of a Love SAW sensor applicable in liquids. Adding a so called wave guiding layer (e.g. SiO_2) may transform a Rayleigh wave device into a Love wave device.

In addition to the detection of molecules, the detection of heavier objects (receptors and bio objects) like DNA, aptamers, pathogens and bacteria is also a challenge and, due to numerous applications, also extremely interesting for the developed technology. The analysis of the sensitivity of LNO and KNNO has shown that the maximum sensitivity of SAW devices actually lies at higher mass loads and/or frequencies. Moreover, detection in liquids is difficult with Rayleigh waves since the vertical motion component of the wave is strongly attenuated. However, by adding a wave guiding layer (e.g. an additional ~ 630 nm or ~ 130 nm thick SiO_2 layer for the LNO or KNNO, respectively), the generation of so called Love Waves (dispersive shear horizontal waves) can be induced, which would make the sensor applicable for liquids and at the same time much more sensitive (nearly a factor 9 larger sensitivity is expected). It definitely would be challenging to try this and convert the existing sensor (especially the KNNO SAW) to a more sensitive Love Wave sensor (see Figure 48).

Appendices

Appendix A
Sample lists

Table 5: Investigated PLD prepared KNNO thin films, size (10 x 10) mm^2

Name	Film composition	Film thickness	$d_\perp$	Substrate	Sample design
DP_1345	$K_{0.7}Na_{0.3}NbO_3$	22 nm	4.065 Å	$DyScO_3$	Twist180g2
DP_1347	$K_{0.9}Na_{0.1}NbO_3$	(30 nm)[a]	4.016 Å	$TbScO_3$	Twist180g2
DP_1349	$K_{0.3}Na_{0.7}NbO_3$	22 nm	3.961 Å	$TbScO_3$	Twist180g2
DP_1353	$K_{0.1}Na_{0.9}NbO_3$	42 nm	3.9099 Å	$TbScO_3$	Twist180g2
DP_1695	$K_{0.9}Na_{0.1}NbO_3$	31 nm	4.05 Å	$TbScO_3$	Twist180g3
DP_1698	$K_{0.9}Na_{0.1}NbO_3$	34 nm	4.04 Å	$GdScO_3$	Twist180g3

Table 6: Investigated MOCVD prepared KNNO thin film, size (10 x 10) mm^2

Name	Film composition	Film thickness	$d_\perp$	Substrate	Sample design
47_008_SSO	$K_{0.7}Na_{0.3}NbO_3$	31 nm	4.0635 Å	$SmScO_3$	Liang_2017

Table 7: LNO sample list, thickness 0.5 mm, size (10x10) mm^2

Name	Material	Sample design
Windmill 1_500L (YX)	$LiNbO_3$ – Y-cut	Windmill_500L
Windmill 2_500L (YX)	$LiNbO_3$ – Y-cut	Windmill_500L
Windmill 3_1000L (YZ)	$LiNbO_3$ – Y-cut	Windmill_1000L
Windmill 4_250L (YX)	$LiNbO_3$ – Y-cut	Windmill_250L
Windmill 5 (YX)	$LiNbO_3$ – Y-cut	Windmill_500L
LNO_500_Tw90_1	$LiNbO_3$ – Y-cut	Twist90
LNO_500_Tw90_2	$LiNbO_3$ – Y-cut	Twist90
LNO_500_Tw180_1	$LiNbO_3$ – Y-cut	Twist180
LNO_500_Tw180_2	$LiNbO_3$ – Y-cut	Twist180
LNO_503_Tw180g2_1	$LiNbO_3$ – Y-cut	Twist180g2
LNO_503_Tw180g2_2	$LiNbO_3$ – Y-cut	Twist180g2
LNO_503_Tw180g3_3	$LiNbO_3$ – Y-cut	Twist180g3
LNO_503_Tw180g3_4	$LiNbO_3$ – Y-cut	Twist180g3
LNO_503_Tw180g3_5	$LiNbO_3$ – Y-cut	Twist180g3
LNO_503_Tw180g3_6	$LiNbO_3$ – Y-cut	Twist180g3

Appendix B
Sample designs

Windmill

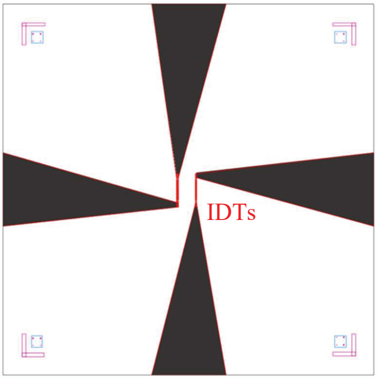

$W = D =$ 250 µm, 500 µm, 1000 µm

$\lambda = 12$ µm

Twist90

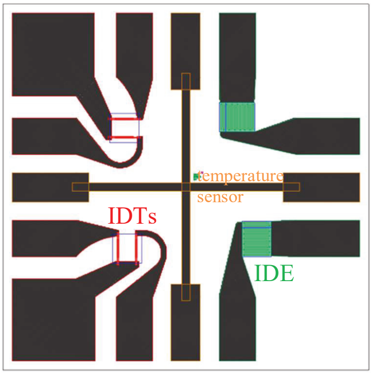

$W = D =$ 500 µm

$\lambda = 12$ µm

Twist180, Twist180g2 and Twist180g3

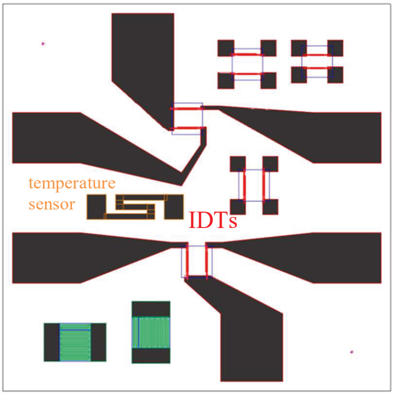

Twist180/Twist180g2, Twist180g3

$W = D =$ 500/504 µm

$\lambda = 12$ µm

Twist180g4

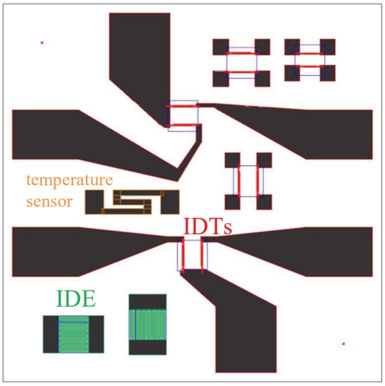

$W = D =$ 498 µm

$\lambda = 12$ µm

(arrangement of digits changed for enhanced bias tunability)

References

[1] D. Ballantine, R. M. White, S. J. Martin, A. J. Ricco, E. T. Zellers, G. C. Frye and H. Wohltjen, Acoustic Wave Sensors: Theory, Design and Physio-Chemical Applications, USA: ACADEMIC PRESS, INC., 1997.

[2] R. M. White and F. W. Voltmer, “Direct piezoelectric coupling to sufrace elastic waves,” *Applied physics letters,* vol. 7, no. 12, pp. 314-316, 1965.

[3] C. Campbell, Surface Acoustic Wave Devices and Their Signal Processing Applications, USA: Academic Press Inc., 1989.

[4] R. Wallis and G. Stegeman, Electromagnetic surface excitations, Italy: Springer, 1985.

[5] T. I. Browning and F. G. Marshall, “Compact 130 microseconds Surface Acoustic Wave delay line using improved MSC reflecting trackchangers,” *Ultrason. Symp.,* pp. 189-192, November 1974.

[6] H. Wohltjen, “Mechanism of operation and design considerations for surface acoustic wave device vapour sensors,” *Sensors and Actuators,* pp. 307-325, 21 May 1984.

[7] B. A. Auld, Acoustic fields and waves in solids, USA: Wiley, 1973.

[8] Allresist GmbH, 24 October 2019. [Online]. Available: https://www.allresist.de/. [Accessed 24 October 2019].

[9] Y. Dai, Tailoring the electronic properties of epitaxial oxide films via strain for SAW neuromorphic accplications, Jülich: Forschungszentrum Jülich GmbH, 2018.

[10] National Center for Biotechnology Information, [Online]. Available: https://pubchem.ncbi.nlm.nih.gov/source/hsdb/5767#section=Environmental-Fate-Exposure-Summary. [Accessed 7 November 2019].

[11] A. Duk, Relationships between strain, ferro- and piezoelectric properties in functional oxide thin films, Humboldt-Universitaet zu Berlin, 2013.

Acknowledgments

This work was initiated and supported by **Research Center Juelich GmbH**.

Also substantial was the close cooperation with the **IKZ Berlin** and the **HNF** (Helmholtz Nano Facility. Journal of large scale research facilities, 3, A112. http://dx.doi.org/10.17815/jlsrf-3-158)

In particular, **Manuel Glaß, Leonard von Helden, Rolf Kutzner, Sijia Liang, Andreas Offenhäusser, Daniel Pfützenreuter, Jutta Schwarzkopf, Nikolaus Wolf, Roger Wördenweber** and **Xiaobo Yuan,** have contributed to this project. I am very grateful for their great ideas, inspiring conversations, helpfulness, criticism, technical and experimental support, time, trust and patience. Thank you

Band / Volume 202
Current-induced magnetization switching in a model epitaxial Fe/Au bilayer
P. Gospodarič (2019), vi, 120, XXXVIII pp
ISBN: 978-3-95806-423-2

Band / Volume 203
Network architecture and heme-responsive gene regulation of the two-component systems HrrSA and ChrSA
M. Keppel (2019), IV, 169 pp
ISBN: 978-3-95806-427-0

Band / Volume 204
Spin-orbitronics at the nanoscale: From analytical models to real materials
J. Bouaziz (2019), 228 pp
ISBN: 978-3-95806-429-4

Band / Volume 205
Advanced methods for atomic scale spin simulations and application to localized magnetic states
G. P. Müller (2019), xx, 194 pp
ISBN: 978-3-95806-432-4

Band / Volume 206
Different growth modes of molecular adsorbate systems and 2D materials investigated by low-energy electron microscopy
J. E. Felter (2019), vi, 114, XXXIV pp
ISBN: 978-3-95806-434-8

Band / Volume 207
NADPH-related studies performed with a SoxR-based biosensor in *Escherichia coli*
A. Spielmann (2019), IV, 73 pp
ISBN: 978-3-95806-438-6

Band / Volume 208
Chemisorption aromatischer Moleküle auf Übergangsmetalloberflächen: Bildung molekularer Hybridmagnete
S. Schleicher (2019), 109 pp
ISBN: 978-3-95806-442-3

Band / Volume 209
Regulatory interactions between *Corynebacterium glutamicum* and its prophages
M. Hünnefeld (2019), IV, 209 pp
ISBN: 978-3-95806-445-4

Band / Volume 210
Quantum Technology
Lecture Notes of the 51st IFF Spring School 2020
23 March – 03 April 2020, Jülich, Germany
ed. by H. Bluhm, T. Calarco, D. DiVincenzo (2020), ca. 700 pp
ISBN: 978-3-95806-449-2

Band / Volume 211
Interaction of physical fields with nanostructured materials
(2020), 255 pp
ISBN: 978-3-95806-450-8

Band / Volume 212
First-principles study of collective spin excitations in noncollinear magnets
F.J. dos Santos (2020), 270 pp
ISBN: 978-3-95806-459-1

Band / Volume 213
Direct measurement of anisotropic resistivity in thin films using a 4-probe STM
T. Flatten (2020), viii, 129 pp
ISBN: 978-3-95806-460-7

Band / Volume 214
The guided self-assembly of magnetic nanoparticles into two- and three- dimensional nanostructures using patterned substrates
W. Ji (2020), VI, 140 pp
ISBN: 978-3-95806-462-1

Band / Volume 215
Molecular layer deposition and protein interface patterning for guided cell growth
M. Glass (2020), iv, 81 pp
ISBN: 978-3-95806-463-8

Band / Volume 216
Development of a surface acoustic wave sensor for in situ detection of molecules
D. Finck (2020), 63 pp
ISBN: 978-3-95806-464-5

Weitere ***Schriften des Verlags im Forschungszentrum Jülich*** unter
http://wwwzb1.fz-juelich.de/verlagextern1/index.asp

Schlüsseltechnologien / Key Technologies
Band / Volume 216
ISBN 978-3-95806-464-5

Mitglied der Helmholtz-Gemeinschaft

JÜLICH
Forschungszentrum